

Rowan University

Rowan Digital Works

Theses and Dissertations

12-31-2002

Automated segmentation of radiodense tissue in digitized mammograms using a constrained Neyman-Pearson classifier

Jeremy Thomas Neyhart
Rowan University

Follow this and additional works at: <https://rdw.rowan.edu/etd>



Part of the [Electrical and Computer Engineering Commons](#)

Recommended Citation

Neyhart, Jeremy Thomas, "Automated segmentation of radiodense tissue in digitized mammograms using a constrained Neyman-Pearson classifier" (2002). *Theses and Dissertations*. 1492.
<https://rdw.rowan.edu/etd/1492>

This Thesis is brought to you for free and open access by Rowan Digital Works. It has been accepted for inclusion in Theses and Dissertations by an authorized administrator of Rowan Digital Works. For more information, please contact graduateresearch@rowan.edu.

**Automated segmentation of radiodense tissue in digitized mammograms using a
constrained Neyman-Pearson classifier**

by

Jeremy Thomas Neyhart

A Thesis Submitted to the
Graduate Faculty in Partial Fulfillment of the
Requirements for the Degree of
MASTER OF SCIENCE

Department: Electrical and Computer Engineering
Major: Engineering (Electrical Engineering)

Approved:

Members of the Committee

In Charge of Major Work

For the Major Department

For the College

Rowan University
Glassboro, New Jersey
2002

ABSTRACT

Jeremy Thomas Neyhart

Automated segmentation of radiodense tissue in digitized mammograms using a constrained Neyman-Pearson classifier

2002

Dr. Shreekanth Mandayam
College of Engineering

Breast cancer is the second leading cause of cancer related mortality among American women. Mammography screening has emerged as a reliable non-invasive technique for early detection of breast cancer. The radiographic appearance of the female breast consists of radiolucent (dark) regions and radiodense (light) regions due to connective and epithelial tissue. It has been established that the percentage of radiodense tissue in a patient's breast can be used as a marker for predicting breast cancer risk. This thesis presents the design, development and validation of a novel automated algorithm for estimating the percentage of radiodense tissue in a digitized mammogram. The technique involves determining a dynamic threshold for segmenting radiodense indications in mammograms. Both the mammographic image and the threshold are modeled as Gaussian random variables and a constrained Neyman-Pearson criteria has been developed for segmenting radiodense tissue. Promising results have been obtained using the proposed technique. Mammograms have been obtained from an existing cohort of women enrolled in the Family Risk Analysis Program at Fox Chase Cancer Center (FCCC). The proposed technique has been validated using a set of ten images with percentages of radiodense tissue, estimated by a trained radiologist using previously established methods. This work is intended to support a concurrent study at the FCCC exploring the association between dietary patterns and breast cancer risk.

MINI - ABSTRACT

Jeremy Thomas Neyhart

**Automated segmentation of radiodense tissue in digitized mammograms using a
constrained Neyman-Pearson classifier**

2002

Dr. Shreekanth Mandayam
College of Engineering

An automated technique for the segmentation of radiodense tissue in digitized mammograms was developed. The results were validated by a trained radiologist using an accepted technique with images provided by Harvard Medical School.

TABLE OF CONTENTS

List of Figures	iv
List of Tables	vii
Abstract.....	viii
Acknowledgements.....	ix
Chapter 1: Introduction.....	1
1.1 Medical Imaging.....	1
1.1.1 Enhancement.....	2
1.1.2 Segmentation.....	2
1.1.3 Quantification.....	3
1.1.4 Visualization.....	3
1.2 Medical Imaging In Mammography.....	4
1.3 Mammography Procedure.....	8
1.4 Statement of the Problem	11
1.5 Objectives and Scope of the Thesis	13
Chapter 2: Background.....	14
2.1 Background of Breast Density Research.....	14
2.1.1 Origin of breast density as a risk factor.....	14
2.1.2 “Toronto” method: six-category classification	14
2.1.3 Interactive Segmentation.....	16
2.1.4 Automatic segmentation techniques.....	18
2.1.5 Symmetry of view.....	19
2.1.6 Segmentation of radiodense tissue using fuzzy connectivity.....	20
Chapter 3: Modeling and segmentation of Gaussian random images	22
3.1 Introduction.....	22
3.2 Image Modeling.....	22
3.2.1 Random variables used.....	24
3.2.2 Canonical images.....	25
3.3 Classical Image Segmentation Techniques.....	28
3.3.1 Bayesian classifier.....	28
3.3.2 Neyman-Pearson classifier.....	29
Chapter 4: Approach.....	32
4.1 Introduction.....	32
4.2 Digitization and Pre-processing.....	33
4.3 Mask Generation.....	35
4.3.1 Generation of segmentation mask.....	35

4.3.1.1	Discrete wavelet transform	37
4.4	Tissue Segmentation.....	39
4.5	Threshold Determination.....	40
4.5.1	Image modeling.....	41
4.5.2	Radiodense tissue segmentation.....	42
4.5.2.1	Image segmentation by modeling the threshold as a random variable.....	42
4.5.2.2	Bayesian segmentation approach.....	44
4.5.2.3	Augmented Bayesian segmentation approach.....	44
4.5.2.4	Constrained Neyman-Pearson segmentation approach.....	45
4.6	Density Estimation and Image Post-Processing.....	46
Chapter 5: Results.....		47
5.1	Introduction.....	47
5.2	Mask Generation and Tissue Segmentation Techniques.....	47
5.3	Radiodense Tissue Segmentation algorithms.....	50
5.3.1	Image segmentation by modeling the threshold as a random variable	50
5.3.2	Algorithm modification based on validation data.....	53
5.3.2.1	Blind classification.....	54
5.3.2.1.1	Initial threshold determination.....	54
5.3.2.1.2	Initial determination of scaling parameters.....	55
5.3.2.1.3	Results.....	55
5.3.2.2	Supervised classification.....	56
5.3.2.2.1	Automated initial threshold determination.....	57
5.3.2.2.2	Determination of the scaling parameter, α	58
5.3.2.2.3	Results.....	59
Chapter 6: Conclusions.....		70
6.1	Summary of Accomplishments.....	71
6.2	Recommendations for Future Work.....	73
References.....		74
Appendix: Matlab Code.....		77

LIST OF FIGURES

- FIGURE 1.1** – Mammogram X-ray with (a) radiodense and (b) radiolucent tissue labeled, and (c) film (non-tissue) region. **6**
- FIGURE 1.2** – Proper positioning of the (a) craniocaudal and (c) mediolateral oblique views of the breast and (b) and (d) their respective mammographic films. **10**
- FIGURE 1.3** – Four representative images showing (a) low radiodensity; bright image, (b) high radiodensity; bright image, (c) low radiodensity; dark image and (d) high radiodensity; dark image. **12**
- FIGURE 2.1** – Block diagram of the Toronto interactive computer method for determination of radiodense tissue percentages. This method uses two grayscale thresholds to determine tissue/film boundary and radiodense/radiolucent boundary. **17**
- FIGURE 2.2** - (a) CC and (b) MLO views of the same breast, shows the appearance of the pectoral muscle in the MLO view. **19**
- FIGURE 3.1** – (a) Original image and (b) modeled image using 4 x 4 local regions. Image size is 512 x 512 pixels. **23**
- FIGURE 3.2** – (a) CDF of a Gaussian random field and (b) derivative of the CDF which is the PDF of the Gaussian random field. **24**
- FIGURE 3.3** – (a) Gaussian random field of range {0,255}, (b) plot of percentage of black pixels while varying segmentation threshold across entire range shows the CDF of the random field, (c) the differentiation of the CDF of the random field is the PDF and (d) result of segmenting (a) about the mean of the PDF results in $P[\text{white}] = P[\text{black}] = 0.5$. **26**
- FIGURE 3.4** – (a) Three canonical random Gaussian fields. Images 1 and 3 have means higher and lower than the median respectively. (b) Images segmented about the median and (c) segmented about the mean of their individual PDF. The probability of white and black pixels is approximately equal in each image in (c). **27**
- FIGURE 3.5** – Illustration of two distributions with Bayesian classifier segmentation threshold, T_B , labeled. Note the minimization of classification error for both distributions. **29**
- FIGURE 3.6** - Illustration of two distributions with Neyman-Pearson classifier segmentation threshold, T_{NP} , labeled. Note the classification bias towards the mean of the second distribution, μ_2 . **30**

FIGURE 4.1 - Overall approach breast density estimation.	32
FIGURE 4.2 - Flow diagram of research approach.	33
FIGURE 4.3 - (a) CC and (b) MLO views of the same breast, shows the appearance of the pectoral muscle in the MLO view.	34
FIGURE 4.4 - (a) Original mammogram image and (b) line-scan of single row of the image as indicated by the line placed on the original image.	36
FIGURE 4.5 – (a) Typical image and (b) automatically created segmentation mask.	36
FIGURE 4.6 - Multiresolution wavelet decomposition tree.	38
FIGURE 4.7 - A typical line-scan and corresponding 5 th level DWT approximation coefficients.	38
FIGURE 4.8 - Tissue segmentation results for a typical image – (a) original X-ray (b) boundary estimation (c) mask generation (d) tissue segmented image.	39
FIGURE 4.9 – (a) Original mammogram image and (b) its Gaussian random model. Note that the segmentation mask has been applied to (b) using the techniques described earlier.	41
FIGURE 4.10 - (a) Effect of varying segmentation threshold on the percentage of black pixels in a gray-level mammogram image and (b) Probability density function of the threshold random variable.	43
FIGURE 5.1 - Four sets of data showing (a) the original image, (b) edge of tissue region, (c) associated mask and (d) image and mask combined.	48
FIGURE 5.2 – Histogram of tissue region of typical image from the FCCC dataset showing the low intensity values that characterize these images.	51
FIGURE 5.3 - Typical results showing (a) the original image and (b-e) the binary segmented tissue region resulting from $\alpha = 0.65, 0.75, 0.85, 0.95$ respectively for three patients.	52
FIGURE 5.4 – Histogram of an image provided by Dr. Celia Byrne. Comparison to Figure 5.2 reveals the differences in the tow datasets intensity values.	53
FIGURE 5.5 – Gaussian distribution of pixel intensities showing the regions considered “dark” and “bright.”	58

FIGURE 5.6 – Actual percentage of radiodense tissue and percentage of radiodense tissue calculated using the best-matched threshold from Table 6.5.	61
FIGURE 5.7 – Segmented images using 127% initial threshold. This method segments 19131709, 20110811, 11599502 with minimal classification error.	62
FIGURE 5.8 – Threshold resulting from analysis of image using 127% initial threshold.	63
FIGURE 5.9 – Percentage of radiodense tissue resulting from analysis of image using 127% initial threshold.	63
FIGURE 5.10 – Segmented images using 115% initial threshold. This method segments 15839502, 11051702, 26253102, 28657701 with minimal classification error.	64
FIGURE 5.11 - Threshold resulting from analysis of image using 115% initial threshold.	65
FIGURE 5.12 - Percentage of radiodense tissue resulting from analysis of image using 115% initial threshold.	65
FIGURE 5.13 – Segmented images using 80% of initial threshold. This method segments 27786202 and 26799401 with minimal classification error.	66
FIGURE 5.14 - Threshold resulting from analysis of image using 80% initial threshold.	67
FIGURE 5.15 - Percentage of radiodense tissue resulting from analysis of image using 80% initial threshold.	67

LIST OF TABLES

TABLE 1.1 – Breast cancer risk factors from [12].	5
TABLE 2.1 – Summary of work in breast density analysis.	15
TABLE 5.1 - Percentage and mean square error from manually developed reference mask for patients from Figure 6.1.	49
TABLE 5.2 - Summary of percentages of radiodense tissue for patients from Figure 5.3.	51
TABLE 5.3 – Blind Segmentation Rank using each method and actual rank provided afterwards by Dr. Byrne.	56
TABLE 5.4 - Validation Images and associated data; ranked by increasing radiodense percentage.	60
TABLE 5.5 - Validation threshold, T_v , and the final threshold determined for each initial threshold.	68
TABLE 5.6 – Percentage error for the final threshold determined for each initial threshold. Uses $ (T_v - T_{CMP})/T_v *100\%$.	68
TABLE 5.7 - Actual percentage of radiodense tissue and amount calculated for each initial threshold.	69
TABLE 5.8 - Percentage error for the calculated radiodense tissue percentage determined for each initial threshold. Uses $ (T_v - T_{CMP}) $.	69

ABSTRACT

Breast cancer is the second leading cause of cancer related mortality among American women. Mammography screening has emerged as a reliable non-invasive technique for early detection of breast cancer. The radiographic appearance of the female breast consists of radiolucent (dark) regions and radiodense (light) regions due to connective and epithelial tissue. It has been established that the percentage of radiodense tissue in a patient's breast can be used as a marker for predicting breast cancer risk. This thesis presents the design, development and validation of a novel automated algorithm for estimating the percentage of radiodense tissue in a digitized mammogram. The technique involves determining a dynamic threshold for segmenting radiodense indications in mammograms. Both the mammographic image and the threshold are modeled as Gaussian random variables and a constrained Neyman-Pearson criteria has been developed for segmenting radiodense tissue. Promising results have been obtained using the proposed technique. Mammograms have been obtained from an existing cohort of women enrolled in the Family Risk Analysis Program at Fox Chase Cancer Center (FCCC). The proposed technique has been validated using a set of ten images with percentages of radiodense tissue, estimated by a trained radiologist using previously established methods. This work is intended to support a concurrent study at the FCCC exploring the association between dietary patterns and breast cancer risk.

ACKNOWLEDGEMENTS

My thanks and appreciation go out especially to my advisor, Dr. Shreekanth Mandayam. His encouragement and help throughout this year have been wonderful. He has guided me well and I will always be thankful of the knowledge he has given me and of the friendship we have developed.

Also I would like to thank Dr. Robi Polikar for the help he has given me in my research. His knowledge was a welcome resource. Dr. Anthony Marchese, thank you for serving on my committee and for your advice in revising my thesis. I need to thank the rest of the Engineering faculty who have always been available for consultation and support throughout my stay here. I also wish to acknowledge my fellow graduate students and friends, Michael Ciocco and Glen Roames, who have made this experience quite memorable.

This project was supported by the Fox Chase Cancer Center through grants from the American Cancer Society and the American Institute for Cancer Research. Their support is greatly appreciated. I want to thank Dr. Marilyn Tseng of FCCC who is the principle investigator on the project and Dr. Celia Byrne who was provided validation data and helped to guide our work.

I would like to thank my family who has supported me in all of my goals and who encouraged me to pursue my Master's degree. Thank You. Finally, I wish to thank my Grandmother, a breast cancer survivor who recently passed away, for all of the wisdom and spirit that she shared with me.

CHAPTER 1: INTRODUCTION

Cancer of the human body is one of the most deadly forms of disease. In 1999, It was the second leading cause of death among Americans, accounting for 21.7% of deaths among women and 24.3% of deaths among men [1]. Cancer related disease was second only to heart disease as a cause of death for Americans. As such there is much interest in the detection, diagnosis, treatment and eradication of cancer. For American women breast cancer is particularly pervasive. Breast cancer has consistently been the second leading cause of cancer related mortality among American women [2]. In recent years breast cancer mortality has seen only a slight decline most likely due to early detection by doctors and an overall increase in awareness of patients [3].

1.1 Medical Imaging

The need to analyze the human body is paramount to the advancement of medicine. Medical imaging seeks to analyze the structure, function and pathology of the body using nondestructive techniques. Interrogation methods employ x-rays, ultrasound, magnetic resonance, radioactivity, etc to image the human body. The analysis of images so obtained is used in almost every aspect of health care. As computational power increases, implementing complicated algorithms to perform medical imaging becomes easier. The process of modern medical imaging can be broken into six areas [4];

- 1) Enhancement
- 2) Segmentation
- 3) Quantification
- 4) Registration
- 5) Visualization
- 6) Compression and communication

These areas represent the different tasks that are needed to effectively analyze portions of the body. Since health care providers need to examine every aspect of the body; from the cellular level, to the organs and system level, then no single solution is possible, or practical. Different techniques need to be developed to allow the analysis of specific parts of the body. These operations are not mutually exclusive. For instance, the algorithm proposed in this thesis uses novel techniques in enhancement, segmentation and visualization to perform the required task effectively.

1.1.1 Enhancement

Enhancement improves the visual conditioning of an image. This includes contrast correction and noise reduction. In images, noise can be picked up in the communication channel or be intrinsic to the process. Noise is especially of concern to medical imaging because of the low contrast resulting from many imaging modalities. This noise can easily blur the boundary between normal and abnormal tissue, or between regions of interest and regions of disregard. Enhancement algorithms attempt to reduce this noise and improve the contrast in regions of interest. These algorithms can be used as a stand-alone process, for instance, improving the viewability of an image for a radiologist. They are also used as preprocessing steps for segmentation and quantification algorithms. Proper image enhancement is paramount to a successful medical imaging algorithm.

1.1.2 Segmentation

In medical imaging the captured image often contains more area than needs to be analyzed. When this is the case, the region of interest needs to be segmented so that

further analysis can be performed. This can be accomplished using anything from simple threshold selection or interactive region selection to advanced algorithms using automatic region growing or fuzzy connectedness. The process of segmentation can be considered the most important step in the medical imaging process. This is because the accuracy of the segmentation algorithm has a profound impact on subsequent image processing.

1.1.3 Quantification

Quantification algorithms are used to analyze segmented regions. A number of measurements can be taken from these regions. They can be of a variety of structures and their properties. Because of this diversity, quantification algorithms are task specific. They allow the researcher to make measurements of the human body in a repeatable and consistent manner. The quantification process is highly dependent of the performance on the segmentation algorithms, as proper measurements cannot be made if erroneous data is present. Proper quantification is also highly dependent on the selected features of the region under inspection.

1.1.4 Visualization

Visualization involves the process of displaying data in a usable manner. This can range from color overlays of x-rays to real-time in-situ graphics during a surgery. In the research presented in this thesis the visualization steps seek to highlight the areas under examination. Feature outlining, as well as black and white transformations allow easy, visual, qualitative examination of algorithm performance against known outcomes. This contributes to hasten the development time and improve future analysis.

1.2 Medical Imaging in Mammography

Medical imaging analysis for diagnostic purposes involves the development and implementation of techniques for the detection of malignancies or their pre-cursors. This is a very active area of research, with much of the current work being in the area of microcalcification detection [5 - 8]. Microcalcifications have been shown to be a good indicator of a malignancy in the area of their discovery, accounting for nearly half of the breast cancer detected through mammography techniques [5]. At this time many algorithms have been presented that perform well in segmenting these cancer indications. Methods used in the detection of microcalcifications include multiresolution wavelet analysis [5 - 7], feature based pattern recognition [8] and Bayesian statistical techniques [9]. Other work has focused on the misclassification of film anomalies as microcalcifications [10] and quantifying difficulty of mammogram classification based on image texture analysis [11].

The research work presented in this thesis focuses on risk factor analysis. Risk factors are indications of a patient's potential for developing a disease. The American Cancer Society separates breast cancer risk factors into two broad categories. The categories are those that cannot be changed, and those that can be modified [3]. Risk factors that are beyond the control of the patient include age, race, family history of breast cancer and other similar factors. Those that can be modified are risk factors such as obesity, alcohol consumption, hormone replacement therapy and other lifestyle factors. Table 1.1 gives a listing of some selected breast cancer risk factors and their relative risk from [12]. The knowledge that a radiologist has of risk factor statistics is essential to the early detection and screening of breast cancer.

TABLE 1.1 – Breast cancer risk factors from [12]

Risk Factor	High-risk Group	Low-risk Group	Relative risk
Age	Old	Young	>4.0
Country of Birth	North America, North Europe	Asia, Africa	>4.0
Socioeconomic status	High	Low	2.0-4.0
Marital status	Never Married	Ever Married	1.1-1.9
Place of residence	Urban	Rural	1.1-1.9
Age at first full term pregnancy	> 30 years	< 20 years	2.0-4.0
Age at menopause	Late	Early	1.1-1.9
Age at menarche	Early	Late	1.1-1.9
Weight, postmenopausal	Heavy	Lean	1.1-1.9
Previous breast cancer	Yes	No	2.0-4.0
Benign proliferative disease	Yes	No	2.0-4.0
Previous cancer (ovary or endometrium)	Yes	No	1.1-1.9
Family history (first degree relative)	Yes	No	2.0-4.0
Family History (mother and sister)	Yes	No	>4.0
Radiation to chest	Large Doses	Minimal Doses	2.0-4.0
Parenchymal patterns	Dysplastic	Normal	2.0-4.0

Studies have shown that breast density can be used as a marker for breast cancer risk [13]. The radiographic appearance of the female breast consists of radiolucent (dark) regions due to fat and radiodense (light) regions due to connective and epithelial tissue. Breast density is a measure of the area of the overall breast that is radiodense in appearance. In this thesis the breast density will also be referred to as radiodensity or simply density interchangeably. Figure 1.1 shows the three major regions of interest in the mammogram, the radiodense tissue region, the radiolucent tissue region and the non-tissue film region.

The measured association of breast density to breast cancer risk has been shown to be higher than other, more commonly used, breast cancer risk factors [14, 15]. In particular one study has shown that women with radiodense tissue in more than 60-75% of the breast are at a four to six times greater risk of developing breast cancer than those with lesser densities [16]. This work was done on a large cohort of women enrolled in the

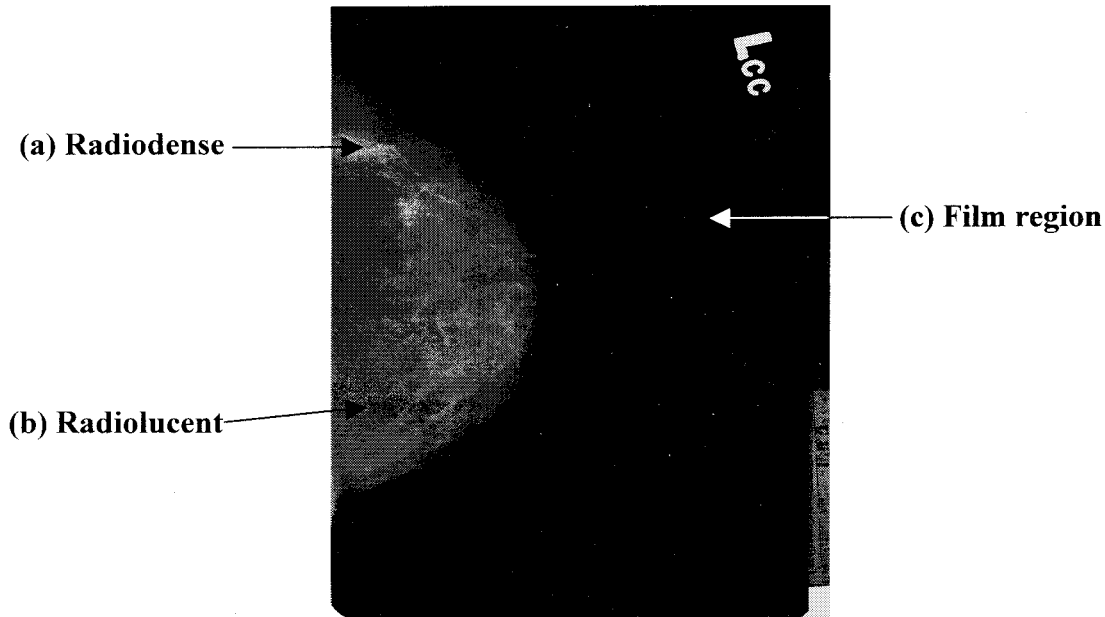


FIGURE 1.1 – Mammogram X-ray with (a) radiodense and (b) radiolucent tissue labeled, and (c) film (non-tissue) region.

Canadian National Breast Screening Study. The estimation of radiodense tissue performed by this study was a subjective determination by trained radiologists.

One of the main hurdles of using breast density to assess a patient's risk of developing cancer is the ability to consistently quantify its amount. Wolfe originally hypothesized that breast density was an indicator of cancer risk [17,18]. He divided mammograms into four groupings; ranging from primarily fatty to primarily dense based on the prominence of the parenchyma. Others have defined ranges of categorization (0%, >0 to <10%, 10 to <25%, 25 to <50%, 50 to <75%, >75% to 100%) that a trained radiologist uses to classify a mammogram [19]. Later work presented a method of quantitatively measuring breast density using digitized mammograms and an interactive computer program [20].

Evidence has been offered that strong correlations exist between breast density and image properties [20]. Two properties that were explored were fractal dimension of an image

[21] and regional skewness[22].

Fractal geometry was originally presented by Mandelbrot [21]. This theory allowed for the description of complex shapes where normal Euclidian geometry fell short. Using fractal geometry, the dimension (similar to spatial dimension) of an object can be calculated. This dimension is a measure of the complexity of an object. When analyzing images, fractal dimension can be used to estimate the smoothness of an image when the image intensities are mapped like a terrain. Reported results show a strong negative correlation between breast density and fractal dimension. This indicating that mammograms of high radiodense tissue are smoother (i.e. more similar) and those of lower radiodense tissue are more rough (i.e. more dissimilar)[23].

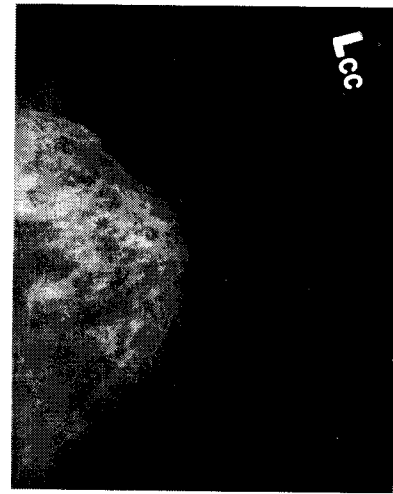
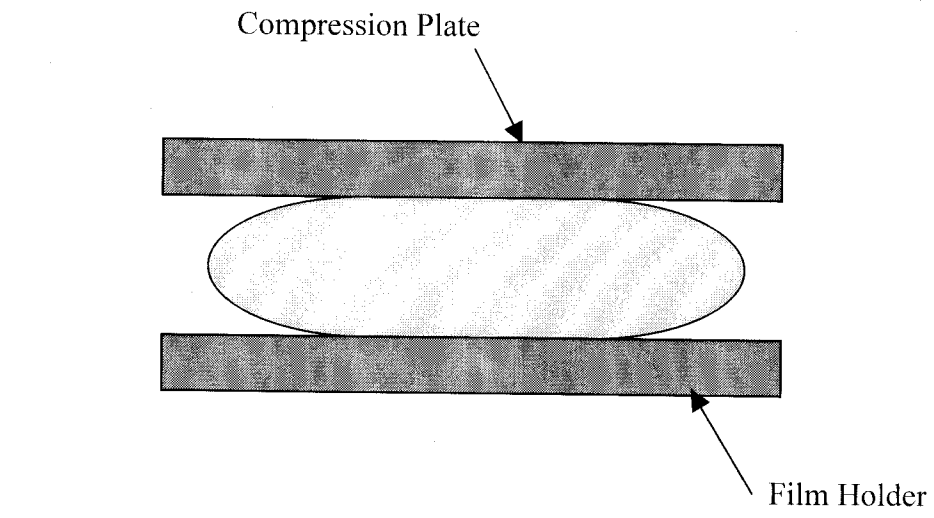
Regional skewness is a measure based on third moment histogram analysis. The histogram of an image is a graph of the quantity of pixels in an image that are of the same value or range of values[22]. The histogram information is irrespective of pixel position and can provide a great deal of information about an image. Information on the skewness of an image is given by the third moment of the image histogram. The method presented used a normalized third moment. It was hypothesized that if a region contains mostly fatty tissue, which is inherently lower in gray level intensity, then it will exhibit a positive skewness. Conversely, those regions that are of a more radiodense nature, which are inherently higher in gray level intensity, will indicate a negative skewness. To provide better resolution, analysis was done using non-overlapping groups of pixels and averaged to provide a single skewness measure. Analysis of this value revealed a strong correlation between skewness and breast density [23].

Although promising results were obtained using both of these means, no quantitative measures of breast density using these techniques were presented. Furthermore, no system for the automatic calculation of the values was presented. The skewness measure required significant user interaction. There is very little published work describing quantitative measures of breast density [20, 24 - 26]. The most promising of which is presented by P.K. Saha *et al.* and involved the automatic segmentation and detection of breast density in digitized mammograms. They used the method of fuzzy connectedness to perform segmentation of different regions. The methods presented in that work will be discussed in detail in Chapter 2.

1.3 Mammography Procedure

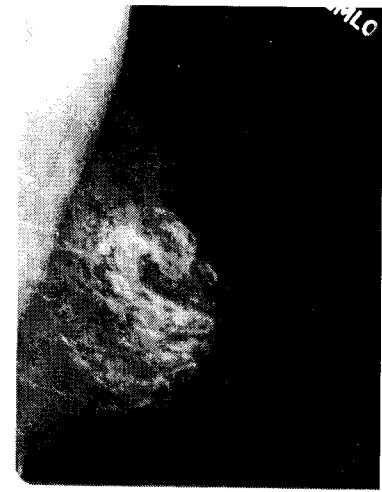
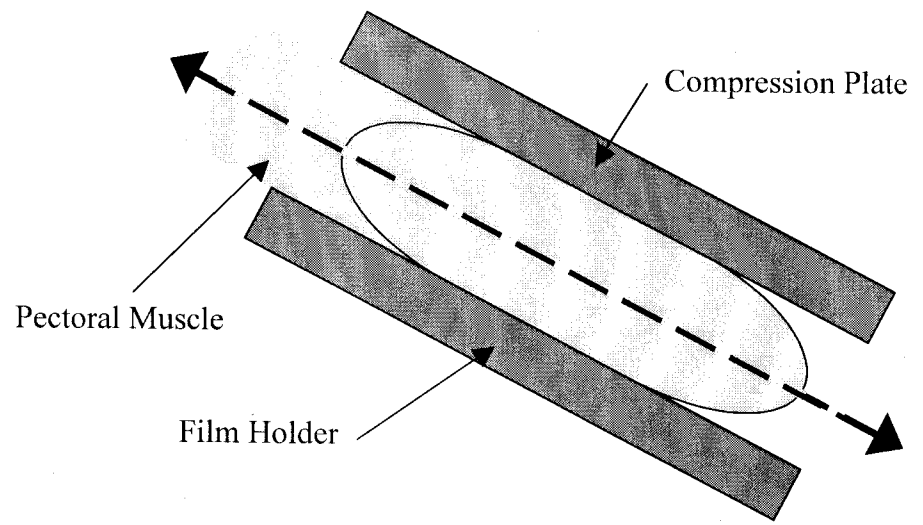
Mammography has been established as a useful non-invasive, low-cost technique for the early detection of breast cancer in women. A mammogram is an x-ray image of a breast taken from one or more views [27]. Typically, each mammogram set contains four x-ray films. The x-rays are of the craniocaudal (CC) and mediolateral oblique (MLO) views of both breasts. The CC view is projected down on the horizontally compressed breast while the MLO view is projected across a breast that is compressed parallel to the patient's pectoral muscle. Figure 1.2 shows the proper positioning of the breast and a representative mammogram for the CC and MLO views respectively. Although much of the x-ray capture process is now automated, proper positioning and compression of the patient's breast by the technologist is essential to capturing a useful set of mammogram films. After the mammogram is taken a trained radiologist traditionally performs the diagnosis of the x-rays. The radiologist is concerned with the presence of immediate

dangers to the patient, malignancy and other abnormalities. Overly high breast density is a concern because of the difficulty it adds to the diagnostic process.



(a)

(b)



(c)

(d)

FIGURE 1.2 – Positioning of the (a) craniocaudal and (c) mediolateral oblique views of the breast and (b) and (d) their respective mammographic films.

1.4 Statement of the Problem

Mammograms x-rays are captured using a semi-automated process. The fact remains that even though there is a great deal of care taken to provide consistent image capture of the mammogram, many variables still exist. One of these variables is the compression of the breast and the positioning. It is obvious that there is an inter-patient variability in the amount of compression and accuracy of positioning that can be accomplished. There exists an intra-patient variability from device to device. It is foreseeable that images of the same patient, all other things being equal, captured on different equipment, will have differing results.

There is significant need for the development of a completely automated system for the segmentation of the radiodense tissue within a mammogram, which is invariant to both inter- and intra-patient variability. The algorithm that is presented must automatically and dynamically adjust a segmentation threshold to eliminate both inter- and intra-patient variability. Mammogram images intensity values can be divided based on two factors; variability due to inter- and intra-patient conditions, and variability due to the prominence and amount of parenchyma in the breast tissue. With this, four cases can be defined that illustrate these issues. They are:

- 1) Low radiodensity; Bright image
- 2) High radio density; Bright image
- 3) Low radiodensity; Dark image
- 4) High radiodensity; Dark image

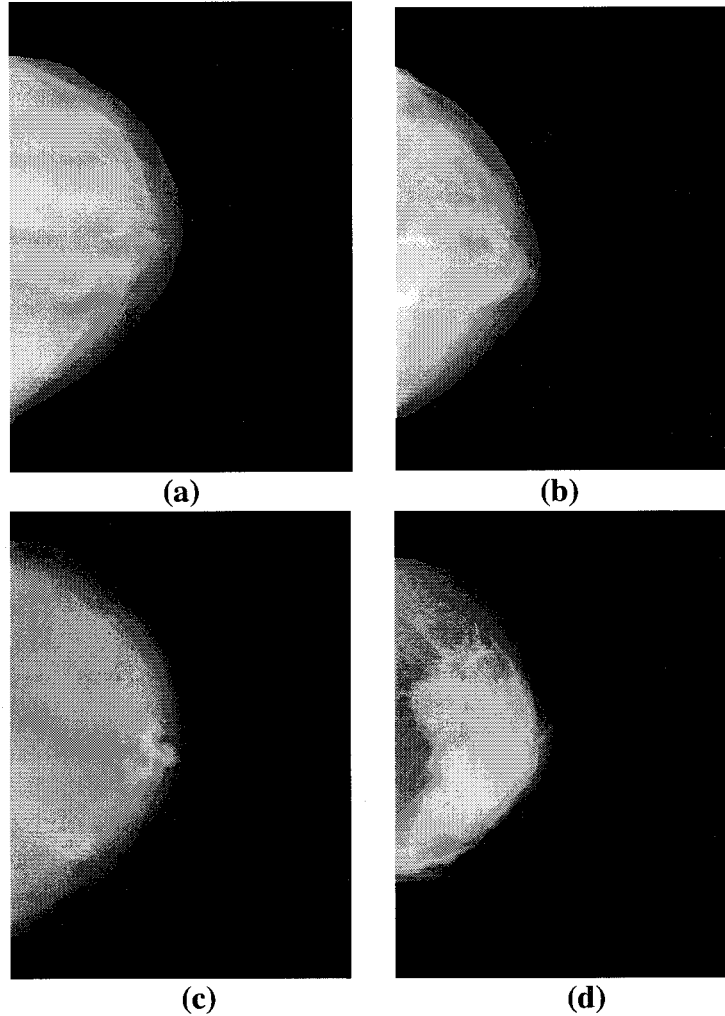


FIGURE 1.3 – Four representative images showing (a) low radiodensity; bright image, (b) high radiodensity; bright image, (c) low radiodensity; dark image and (d) high radiodensity; dark image.

This can be seen in Figure 1.3, which gives an example each type of image. It can be observed that simply choosing a single threshold to classify each image will not suffice. Also, the choice of a simple dynamic threshold, i.e. one that chooses the top 25% of pixel intensity values as radiodense, will be insufficient as well. The research presented here addresses these issues.

1.5 Scope and Organization of the Thesis

This thesis presents a novel algorithm for the automated segmentation and quantification of radiodense tissue in digitized mammograms. Objective measures based on the image gray-level statistics have been developed for tissue segmentation. The primary objective of the research work presented in this thesis is automatic dynamic segmentation of radiodense tissue from within the breast tissue region of a digitized mammogram. The proposed algorithm has been exercised on mammogram images obtained from the Channing Laboratory of the Brigham and Women's Hospital and Harvard Medical School. Results presented in this thesis have been validated by independent assessments from a trained radiologist using previously established methods for assessing radiodensity. This research is intended to support an investigation being conducted at Fox Chase Cancer Center (FCCC), examining the correlation between dietary patterns and breast density.

This thesis is organized as follows, this introduction is followed by a background investigation of mammography and breast density estimation techniques in Chapter 2. Chapter 3 presents a synopsis of techniques from random variable theory that are employed for segmenting known random distributions. The overall approach proposed for automatically segmenting radiodense tissue is presented in Chapter 4. In Chapter 5 the results are presented from exercising the algorithm on the digitized mammograms images. Finally, a summary of the work is provided and future research directions are identified in Chapter 6.

CHAPTER 2: BACKGROUND

2.1 Estimation of Breast Density

Breast density was first proposed as a risk factor for breast cancer in the 1970's by Wolfe [17, 18]. Since then, breast density has been established as a reliable marker for breast cancer risk. There have been several attempts to perform computer-assisted identification and segmentation of radiodense tissue regions in the breast [20, 24, 27, 28]. However, a completely automated algorithm has not yet been developed. This chapter provides a description of prior work in estimating breast density. Table 2.1 summarizes the advances in the estimation techniques.

2.1.1 Origin of breast density as a risk factor

Wolfe proposed that a relationship existed between a patient's radiographic breast density and their risk of developing cancer. Wolfe divided mammography films into four broad categories: those that contained no density and three based on increasing amount of parenchyma, the characteristic tissue of the breast. This method suffered from a great amount of inter- and intra-observer inconsistencies. This was due to the relatively large amount of change required to move a patient from one classification to the next. Another reason was the complete reliance on the subjective assessment of the mammogram by the radiologist.

2.1.2 "Toronto" method: six-category classification

Yaffe, Boyd *et al* have developed a method for determining the percentage of dense tissue in the female breast, often referred to as the "Toronto" method. This method

TABLE 2.1 – Summary of work in breast density analysis.

Proponents	Date	Approach	Data Set
Wolfe [17, 18]	1976	Qualitatively classified breast density into four categories based on the prominence of parenchyma.	
Byng, Boyd, Yaffe, et. al. [19] University of Toronto	1992	Six-Category Classification System. Six categories are defined for breast density; 0%, >0% to <10%, 10% to <25%, 25% to <50%, 50% to <75% and >75% to 100%. Trained radiologist qualitatively performs classification.	Canadian National Breast Screening Study
Byng, Boyd, Yaffe, et. al. [20, 27] University of Toronto	1994	Interactive Segmentation of mammograms using a PC based computer program. Trained radiologists use gray scale thresholds to segment the breast densities	Canadian National Breast Screening Study
Byng, Boyd, et. al. [28] University of Toronto	1996	Proposed automatic analysis of breast density using fractal dimension and regional skewness. Showed strong correlations between these image properties and breast density.	Sub-set of sixty images that span a wide range of breast densities.
Byng, Boyd, Little, et. al. [29] University of Toronto	1996	Analysis of images shows symmetry of view. High correlation between breast density measurements of two views. Allows analysis of only one view	Canadian National Breast Screening Study
Saha, Udupa, et. al. [24] University of Pennsylvania	2001	Automatic Segmentation of breast tissue and breast densities using fuzzy-connectedness model.	60 pairs of CC and MLO views from their database.

builds on the work of Wolfe by separating mammograms into six categories. These categories are 0%, 0 to 10%, 10 to 25%, 25 to 50%, 50 to 75% and 75% to 100%, representing the percentage of radiodense tissue [19]. They offer a more quantitative approach to classification attempts than those offered by Wolfe. A trained radiologist

performs classification of a mammogram into one of the six categories. Although the system allows for a quantitative measure, the classification is still based on the radiologist's qualitative assessment of the mammogram under inspection.

2.1.3 Interactive segmentation

To further reduce reliance on qualitative analysis, while also achieving more precise estimates of breast density, the Yaffe, Boyd *et al* developed a computer program that allows for interactive quantitative analysis of a digitized mammogram [20, 27]. The program allows the radiologist to load a digitized mammogram into the display area of the program. The digitized mammogram is quantified to 12-bits of grayscale information per pixel, which equates to 4096 discrete grayscale levels per pixel. The radiologist uses two separate sliders to choose grayscale thresholds.

The first slider is used to choose the boundary between tissue and film. Using the computer mouse, the radiologist will move the slider to select a threshold. The linear position of the slider is representative of all possible grayscale levels, from 0 (black) to 4096 (white). The selected value is used as a segmentation threshold. As the slider is moved the program overlays a graphical line indicating where the tissue boundary lies. When the radiologist is satisfied that the boundary acceptably outlines the tissue region of the breast they release the slider and move to the second threshold decision slider. The second slider is used to choose the boundary between radiodense and radiolucent tissue. This boundary is chosen in the same way as the first; however, this choice depends on the radiologist's expertise. The training and experience of a particular radiologist allows them to compensate for the variations in gray level intensity from image to image. The

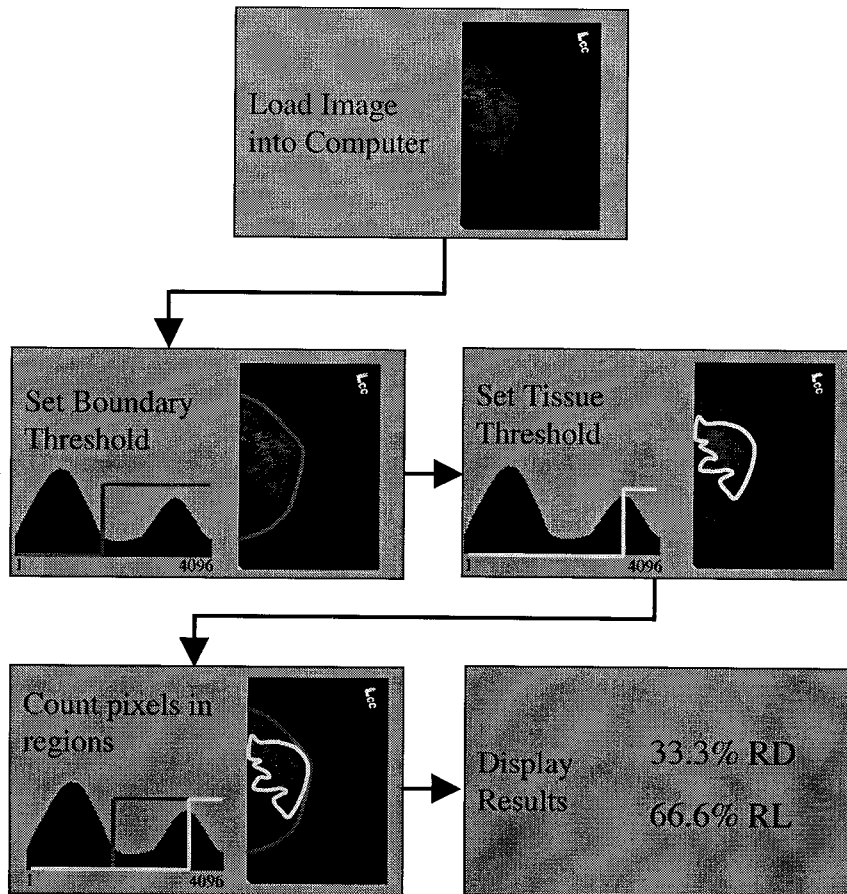


FIGURE 2.1 – Block diagram of the Toronto interactive computer method for determination of radiodense tissue percentages. This method uses two grayscale thresholds to determine tissue/film boundary and radiodense/radiolucent boundary.

researchers state that the use of this simple decision criterion allows for more consistent results from the radiologist and between different radiologists. Figure 2.1 shows a block diagram of the steps taken to analyze the mammogram.

Validation results presented in later chapters were expertly segmented using this technique. Dr. Celia Byrne of the Channing Laboratory, Brigham and Women’s Hospital and Harvard Medical School has provided the segmented validation images.

2.1.4 Automatic segmentation techniques

Additional work by Yaffe, Boyd *et al* proposed possible methods for automatic determination of breast density. They showed that certain image properties were strongly correlated with the amount of radiodensity that was calculated in the breast region by an expert system [28]. Using a subset of 60 images chosen from their database to cover a wide range of radiodensity measurements, they showed strong correlations between both fractal dimension of an image and regional skewness with the calculated amount of breast density in the images as described below.

Fractal geometry was originally defined by Mandelbrot [21]. The analysis of images using fractal methods allows for quantitative measures of the image smoothness over a terrain mapping. Reported results show a strong negative correlation between breast density and fractal dimension, indicating that mammograms with greater radiodense tissue are smoother (i.e. more similar) and those with lower radiodense tissue are rougher (i.e. more dissimilar)[28].

The second method analyzed is the use of the third moment histogram information. This method is known as regional skewness. The hypothesis was presented that if a region contains mostly fatty tissue, which is inherently lower in gray level intensity, then it will exhibit a positive skewness. Conversely, those regions that are of a more radiodense nature, which are inherently higher in gray level intensity, will exhibit a negative skewness. To provide better resolution, analysis was done using non-overlapping groups of pixels and averaged to provide a single skewness measure. Analysis of this value revealed a strong correlation between skewness and breast density [28].

Although promising results were obtained using both methods, no quantitative measures of breast density using these techniques have been presented. Furthermore, no system for the automatic calculation of the system parameters has been presented. Specifically, the skewness measure required the interactive segmentation of the breast tissue region from the rest of the mammography film.

2.1.5 Symmetry of views

The typical mammography film set includes four views; one images each of the CC and MLO view for both breasts. Automatic analysis of the breast is hindered in the MLO view by the inclusion of the pectoral muscle in the x-ray. Automatic segmentation of this muscle would present a difficult challenge. However, it has been shown that the separate analysis of the MLO and CC views results in similar findings of breast density

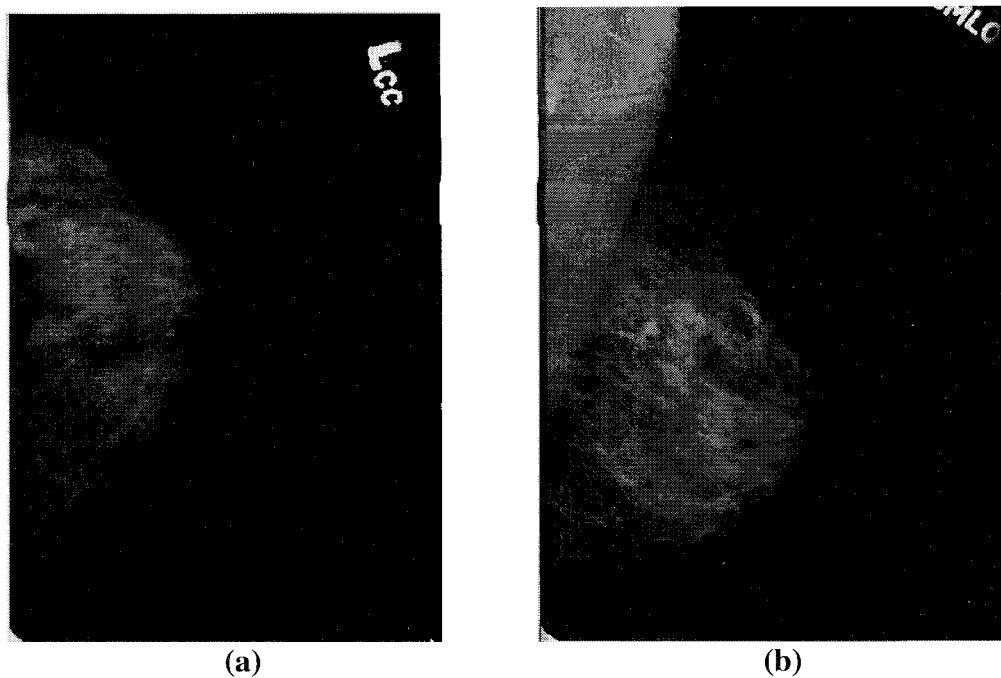


FIGURE 2.2 - (a) CC and (b) MLO views of the same breast, shows the appearance of the pectoral muscle in the MLO view.

[29]. This allows the investigation of only a single view per breast. Because of the inclusion of the pectoral muscle in most MLO views, as shown in Figure 2.2, analysis can now be performed only on the CC views of each x-ray set.

2.1.6 Segmentation of radiodense tissue using fuzzy connectivity

Researchers at the University of Pennsylvania have recently proposed a method for the automatic segmentation of mammographic densities using a fuzzy connectedness [24]. The method of fuzzy connectedness assesses the association of each pixel region to its neighbors. If two regions are found to have a high affinity for each other then they are said to “hang together.” This occurs even when two regions have different intensities. Human vision is analogous to this scheme. A human observer is able to discern the objects in a scene even if regions within that object are not completely homogeneous. The University of Pennsylvania method takes one step to analyze the background of the image and associate all regions within that area. In the second step, the regions of dense tissue are determined. The University of Pennsylvania method requires knowledge of estimated parameters for the region that is to be segmented.

Using the estimated members of the reference region, a so-called “connectedness scene” is created. This scene designates the likeliness for a region to be associated with the reference region. The investigators begin by orienting all images to the left to establish the background location. The upper and lower right corners of the image are chosen as the starting point for the background assignment. This resulting image is then used to create a binary segmentation mask. This allows processing of only the tissue region in further steps. The algorithm is next exercised on the tissue region of the image.

In order to find a reference region, the researchers assigned the highest 32% of intensities found in the histogram of the tissue region as the reference. Results of the algorithm show a strong correlation to segmentation results achieved by a trained radiologist performing manual segmentation.

In this chapter, an overview of previous research work in the area of estimating the breast density, has been presented. Each of these methods offers advancement over past work. The “Toronto” method relies heavily on user input, it is currently the accepted method for segmenting radiodense tissue and will be used as a baseline for comparison of results presented in this thesis. In the following chapter a description of modeling images a collections of Gaussian random fields is presented. An overview of binary segmentation algorithms is also provided.

CHAPTER 3: Modeling and segmentation of Gaussian random images

3.1 Introduction

The following chapter will lay the foundations of image modeling that allow the development of automated segmentation algorithms. The basis for this is the ability to use a Gaussian random field to model an image, which is discussed in the next section. The proposed distribution functions are outlined and canonical images are presented. In Section 3.3 two powerful segmentation algorithms are presented, the Bayesian classifier and the Neyman-Pearson classifier.

Much of the work presented in this chapter is random variable theory. A random variable, X , is a mapping of the results of a random experiment, E , onto the real number line, R . Much information can be realized from the analysis of these random variables and their two-dimensional counterpart, random fields. The reader is referred to ref. [30] for a detailed explanation of random variable theory.

3.2 Image Modeling

The ability to compare different segmentation techniques requires that the image can be modeled mathematically. To create a model, the image is recast as a random field. The image is modeled as a stationary Gaussian random field using the equation

$$f(x, y) = m_f + \sigma_f w(x, y) \quad (3.1)$$

where $f(x, y)$ is the gray-level value in the image at location (x, y) , m_f and σ_f are the local mean and standard deviation of $f(x, y)$ and $w(x, y)$ is a zero-mean, unit variance, Gaussian random field. Empirical evidence suggests that such a model is reasonable for

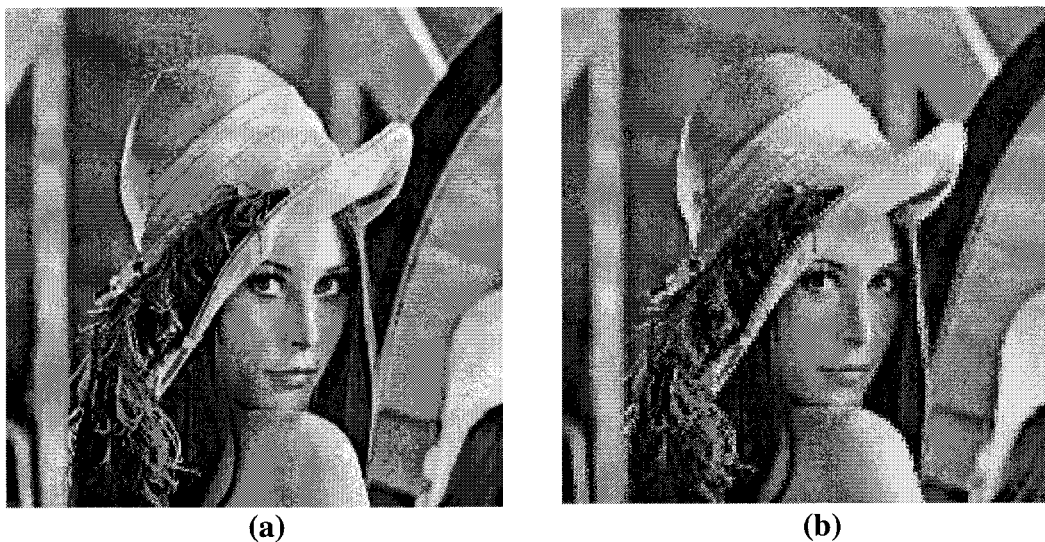


FIGURE 3.1 – (a) Original image and (b) modeled image using 4 x 4 local regions. Image size is 512 x 512 pixels.

typical images [31]. The above prediction holds true if two criteria are met

- (a) The image, $f(x,y)$, is stationary
- (b) The local region modeled is small.

If both of these criteria are met then any image can be modeled as a collection of zero mean, unit variance Gaussian random fields that have been scaled and translated along the real number line using local means and variances. This is illustrated with a canonical image. Figure 3.1 (a) shows the original image and Figure 3.1 (b) shows the modeled image using 4 x 4 local regions and $w(x,y)$ generated using a pseudo random number generator. For this image the region size of 4 x 4 is sufficiently large enough to contain meaningful statistical information and small enough relative to the images 512 x 512 size to fairly accurately model the image.

3.2.1 Random variables used

The Gaussian random variable is chosen for this research as a good candidate for modeling the different portions of tissue that are present in the mammogram. The cumulative distribution function (CDF) of the Gaussian random variable is given as

$$F_x(x) = \frac{1}{1 + e^{-\frac{(x-m)^2}{2\sigma^2}}} \quad (3.2)$$

where the mean, m , is any real number and the variance, σ^2 , is any positive real number [30]. Figure 4.2 (a) plots the Gaussian CDF over a range of inputs, x . The CDF is capable of mapping a possibly infinitely large range of values onto a set range, $[0,1]$ for instance as shown in the figure. Differentiating the CDF produces the probability density function (PDF) of the Gaussian random variable, and is given as

$$f_x(x) = \frac{1}{\sqrt{2\pi}\sigma} e^{-\frac{(x-m)^2}{2\sigma^2}} = N(m, \sigma^2) \quad (3.3)$$

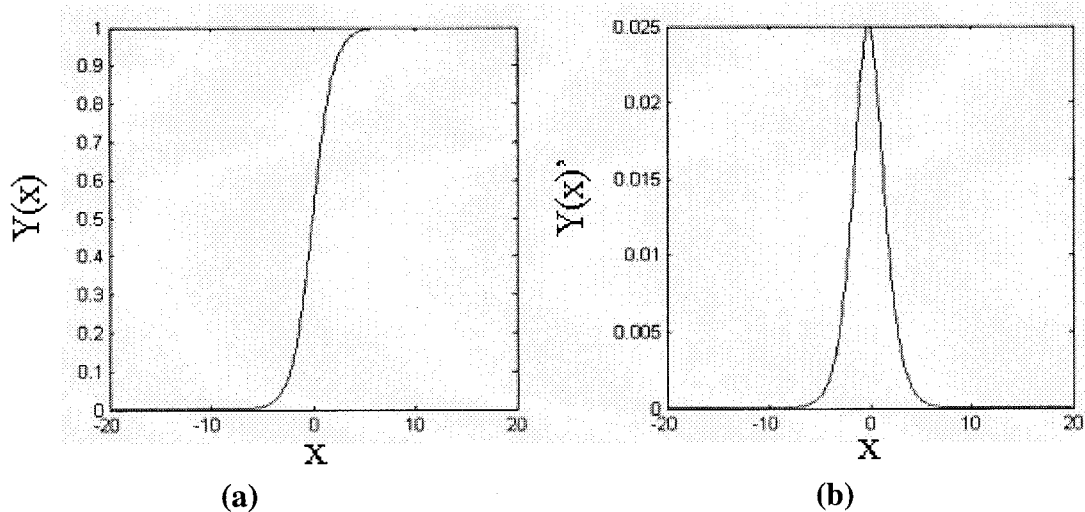


FIGURE 3.2 – (a) CDF of a Gaussian random field and (b) derivative of the CDF which is the PDF of the Gaussian random field.

which is often written as $N(m, \sigma^2)$ to denote a density function of the normal variety. The plot of the PDF is given in Figure 3.2 (b). The PDF shows the probability for the outcome of a random experiment. The mean value of the PDF function, m , is the point of highest probability of the function. For the discrete case it is defined as

$$\mu = \sum_j x_j f(x_j). \quad (3.4)$$

The variance parameter, σ^2 , dictates the spread of the function. For the discrete case it is defined as

$$\sigma^2 = \sum_j (x_j - \mu)^2 f(x_j). \quad (3.5)$$

Using the information that can be extracted from a modeled version of an image, mathematically significant decisions can be made about an image. These decisions can be made automatically and dynamically for any image.

3.2.2 Canonical images

This section will show how statistical information can be used to automatically make decisions about and segment an image. A discrete Gaussian random field is generated

$$f(x, y) = w(x, y) \quad \text{for } x = 0 : 255, y = 0 : 255 \quad (3.6)$$

where $w(x, y)$ is a Gaussian distributed white noise image with range $\{0, 255\}$. The image generated is shown in Figure 3.3 (a). The CDF of the image can be empirically found by performing a series of binary segmentations. If the image is segmented about each point in the range and the percentage of black pixels plotted the result is the CDF of the Gaussian random field, Figure 3.3 (b). Differentiating the CDF gives the PDF of the

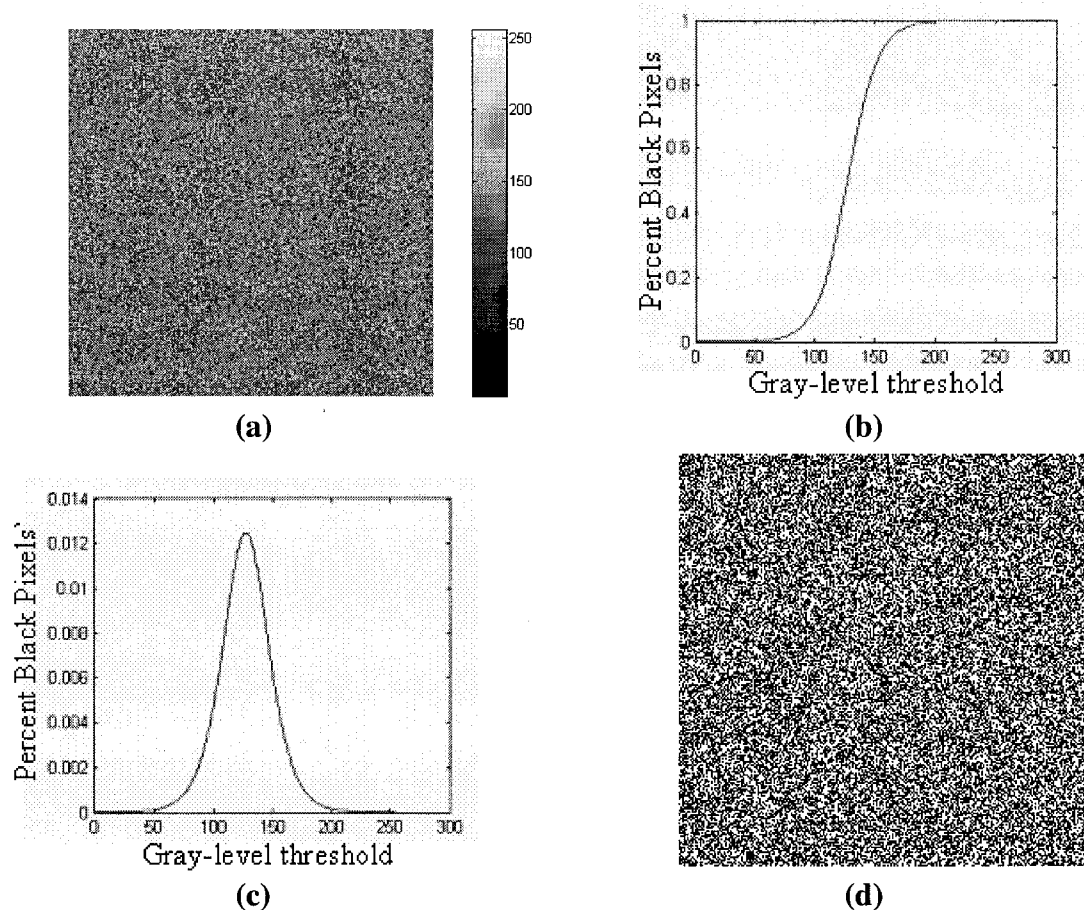


FIGURE 3.3 – (a) Gaussian random field of range $\{0,255\}$, (b) plot of percentage of black pixels while varying segmentation threshold across entire range shows the CDF of the random field, (c) the differentiation of the CDF of the random field is the PDF and (d) result of segmenting (a) about the mean of the PDF results in $P[\text{white}] = P[\text{black}] = 0.5$.

Gaussian random field as seen in Figure 3.3 (c). Finally segmenting this image about the mean of the PDF results in equal probabilities of black and white pixels, Figure 3.3 (d). The resulting Gaussian random field has $m = 128$. This canonical image can be used as a baseline for other image segmentation. The pixels that have an intensity value lower than the mean can be said to be ‘dark’ and those higher than the mean are ‘bright.’

Consider the effect of variation in ambient imaging (lighting) conditions in the choice of the segmentation threshold. This scenario is shown in images 1, 2, and 3 in Figure 3.4 (a), each of which have identical distributions of pixel gray-level values, but

have been imaged in varying lighting conditions.

These three images are converted to binary images by segmenting them using identical thresholds; the resulting binary images are shown in Figure 3.4 (b). These binary images have unequal distributions of black (0) and white (1) pixels. However, if the three images are segmented using a threshold that is set to the mean value of all the pixel gray-level values for each image, the binary images are as shown in Figure 3.4 (c). These three binary images compensate for the variation in imaging conditions and yield equal distributions of black (0) and white (1) pixels.

Essentially this method allows for the proper segmentation of a single density

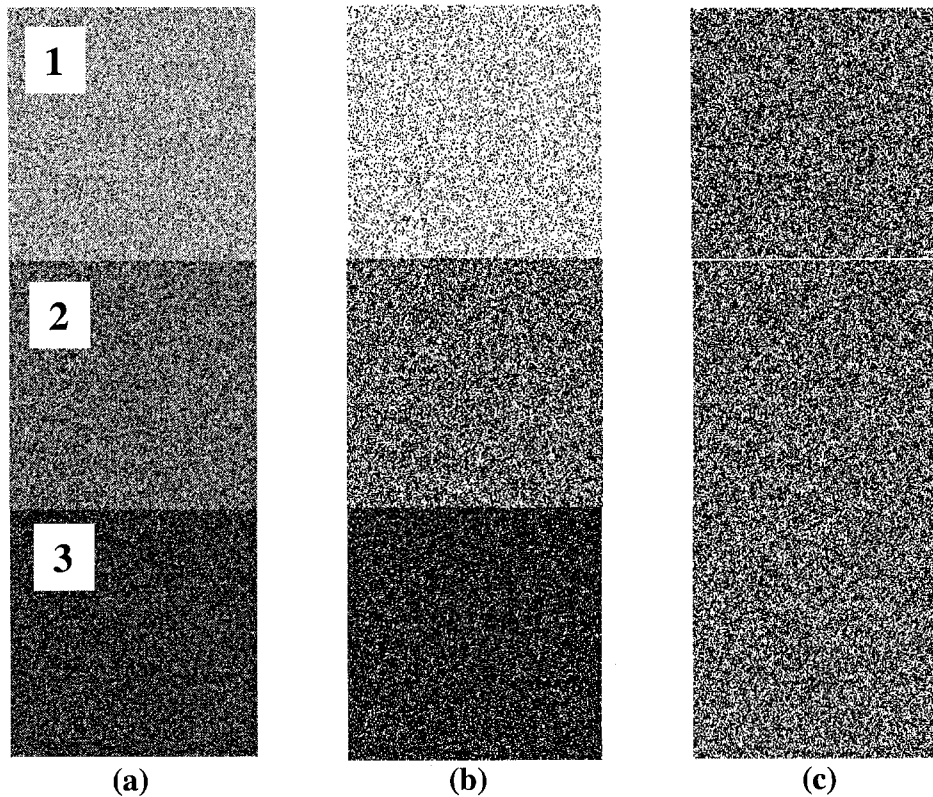


FIGURE 3.4 – (a) Three canonical random Gaussian fields. Images 1 and 3 have means higher and lower than the median respectively. (b) Images segmented about the median and (c) segmented about the mean of their individual PDF. The probability of white and black pixels is approximately equal in each image in (c).

function invariant to the mean of the distribution. This property suggests that this method can be successfully employed to minimize the inconsistencies in testing conditions in mammograms that produce lighter or darker x-ray films.

3.3 Classical Image Segmentation Techniques

The previous sections showed that an image could be modeled as a combination of Gaussian random fields. It also showed that an image, if it is Gaussian in nature, can be automatically and dynamically segmented about the mean of its PDF to divide the image into 'dark' and 'bright' regions. In this section, that concept is built upon with two random field classifiers. Both of these classifiers are based on the statistics of two distributions. The first is the Bayesian classifier; the second is the Neyman-Pearson classifier.

3.3.1 Bayesian Classifier

Baye's decision criterion states that for two distributions that are Gaussian in nature, with equal variance but different means, classification of data can be performed using the following minimum distance function:

$$T_B = \frac{\mu_1 + \mu_2}{2} \quad (3.7)$$

where T_B is the segmentation threshold, μ_1 and μ_2 are the means of the distributions for the two classes. For binary classification, the two classes are '0' and '1'. Class '0' represents the members associated with the distribution of mean μ_1 . The class '1' representing the pixels associated with the distribution of mean μ_2 . Each pixel gray-level

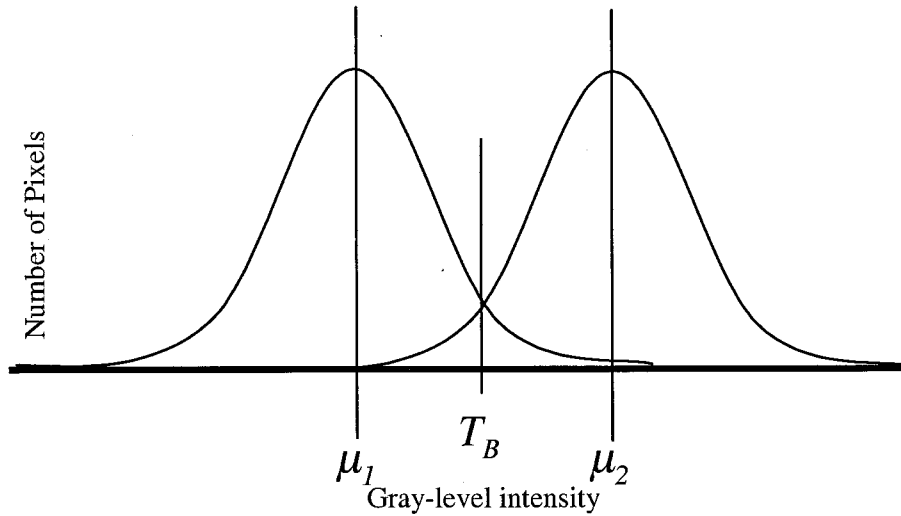


FIGURE 3.5 – Illustration of two distributions with Bayesian classifier segmentation threshold, T_B , labeled. Note the minimization of classification error for both distributions.

value, $f(x, y)$, is compared with the Bayesian threshold, T_B . If $f(x, y)$ is greater than T_B , the pixel is determined to be of class ‘1’ otherwise it is said to be of class ‘0.’ Figure 3.5 illustrates the decision boundary of the Bayesian classifier.

3.3.2 Neyman-Pearson Classifier

The Neyman-Pearson algorithm attempts to improve critical error in classification by providing a bias towards false-positive response. In many situations, it is more desirable to indicate false-positive than false-negative. One example cited in the literature is the air traffic control radar systems [32]. It is more desirable to have a radar system indicate the presence of an aircraft when there is none than to have it indicate no aircraft when one is actually present. The Neyman-Person classifier is given by the equation

$$T_{NP} = \frac{\mu_2 - \mu_1}{2} + \sigma^2 \frac{\eta}{\mu_2 - \mu_1} \quad (3.8)$$

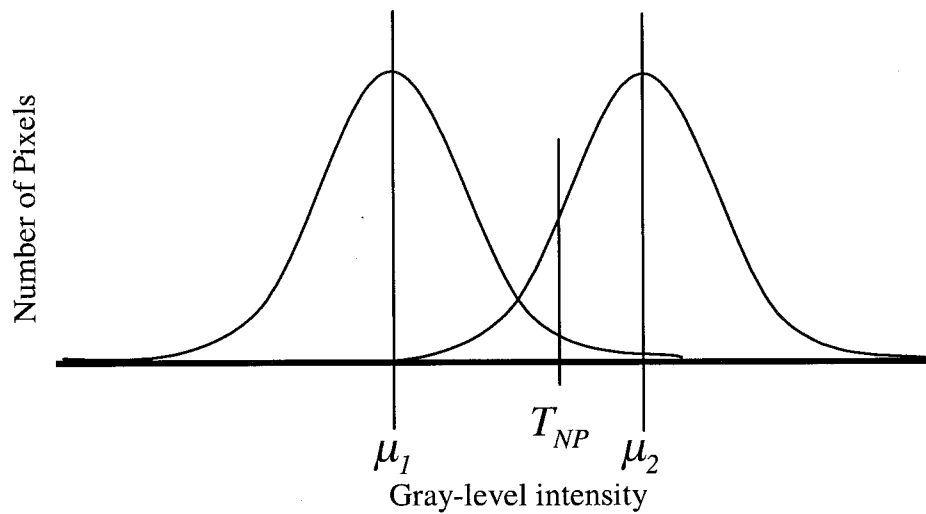


FIGURE 3.6 - Illustration of two distributions with Neyman-Pearson classifier segmentation threshold, T_{NP} , labeled. Note the classification bias towards the mean of the second distribution, μ_2 .

were μ_2 and μ_1 are the means of the two distributions, σ^2 is the variance of the distributions and η is the error minimization parameter. The distribution whose mean is given as μ_2 is known as the null hypothesis. This is the decision with the greatest consequences if not chosen. Cast onto an image segmentation problem the null hypothesis is the area that is being over classified. To this end the Neyman-Pearson technique can be used in any binary classification operation where a bias is desired towards one classification than the other. Figure 3.6 illustrates the threshold, T_{NP} , chosen by the Neyman-Pearson classifier.

The methods presented in this chapter allow for the modeling of an image as a mathematically tractable collection of Gaussian random fields. They also show how variations in the mean can be described by modeling the region to be segmented as a Gaussian random variable. Finally some classical statistical segmentation approaches are

presented.

These methods provide a means for developing an automated segmentation approach based on the underlying statistical properties of a mammogram image. In the following chapter describes the approach used to accomplish this task. The development of a novel algorithm, based of the properties of the Neyman-Pearson classifier, is presented.

CHAPTER 4: APPROACH

4.1 Introduction

The overall research approach is shown in Figure 4.1. A flow diagram demonstrating the process of determining the percentage of radiodense tissue is shown in Figure 4.2. The approach taken addresses two main issues. The first is the actual segmentation of the arbitrarily shaped breast tissue region from within the rectangular shaped x-ray film. This is an edge detection problem that is accomplished using a multiresolution segmentation mask. After the breast tissue is segmented radiodense tissue indications within the breast region can be identified and quantified. The challenge here is that the gray-level intensities vary from x-ray to x-ray and locally across the same x-ray. This is a threshold estimation problem. Several techniques have been developed for dynamically determining a threshold that is capable of segmenting the radiodense tissue.

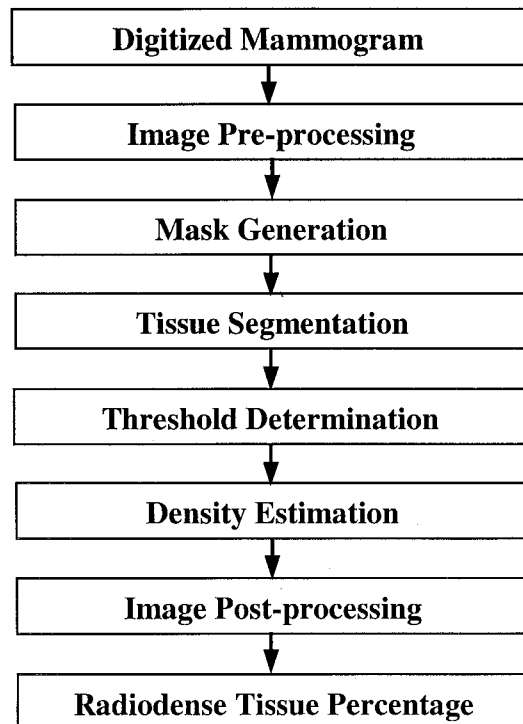


FIGURE 4.1 - Overall approach breast density estimation.

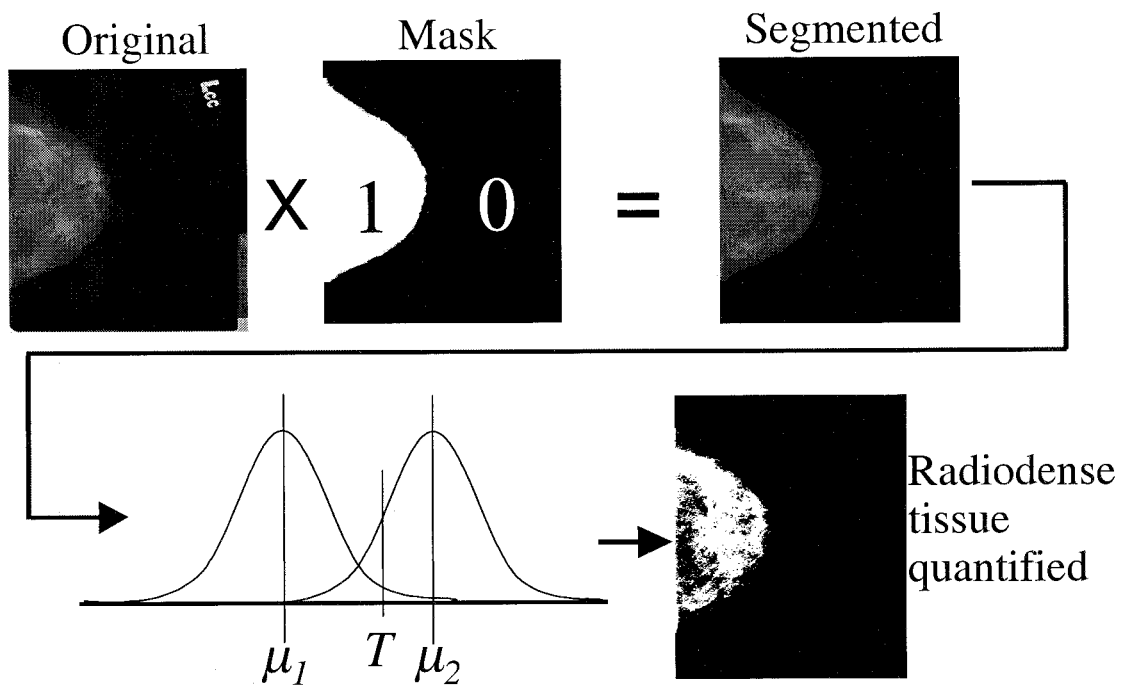


FIGURE 4.2 - Flow diagram of research approach.

Details of these approaches are presented in a later section. The steps taken to implement this research are provided in detail in the following sections.

4.2 Digitization and Pre-processing

The data used in this research comes from the Family Risk Analysis Program at FCCC. This cohort of women includes the daughters, mothers and grandmothers of a population of women that are given regular mammography screenings. Each set of mammograms contains four x-ray films. The x-rays are of the cranio-caudal (CC) and mediolateral oblique (MLO) views of both breasts. The CC view is projected down on the horizontally compressed breast while the MLO view is projected across a breast that is compressed parallel to the patient's pectoral muscle [33]. It has been shown that the separate analysis of the MLO and CC views results in similar findings of breast density

[20]. This allows the investigation of only a single view per breast. Because of the inclusion of the pectoral muscle in most MLO views, as shown in Figure 4.3, analysis is performed only on the CC views of each x-ray set. All x-ray films were digitized at 500 dpi using an Agfa medical-grade film scanner. This resolution was chosen after conducting an extensive survey of existing digital mammography databases [34]-[38]. The digitized image was encoded using 8-bit resolution. An on-line database was created for managing (storing and retrieval) digitized mammogram images at Rowan University. This database, created by Mr. David Chezem of Rowan University Instructional Technologies, uses Macromedia ColdFusion 5.0 [39] and allows secure password-protected access for project team members. The database is indexed using FCCC patient ID, age and date of mammogram.

The first step in image analysis is to map the 8-bit intensity value from the scanner to representative gray scale intensities. Each pixel of data was assigned one of 256 gray-level values ranging from 0 (black) to 1 (white). Each image is oriented to place

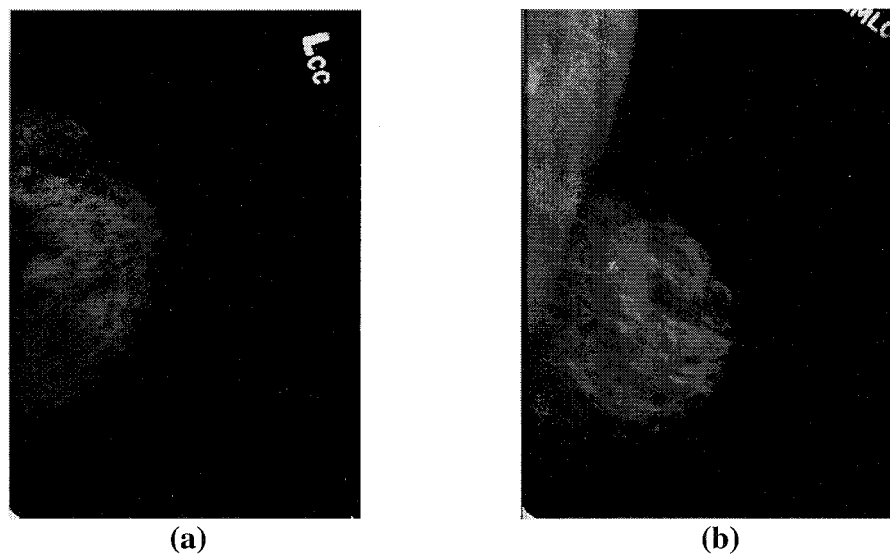


FIGURE 4.3 - (a) CC and (b) MLO views of the same breast, shows the appearance of the pectoral muscle in the MLO view.

the breast region on the left side to further aid automated analysis.

4.3 Mask Generation

To properly quantify the amount and percentage of radiodense tissue present in the breast, there needs to be a technique for separating the tissue region of the x-ray from the film region. To accomplish this, a segmentation mask is used to separate the tissue region from the film region. The mask template is a binary matrix of size equal to that of the original image. The segmentation algorithm described below determines which pixels of the image correspond to a tissue region, and assigns the value 1 (white) to the corresponding regions of the matrix. The rest of the matrix, corresponding to the non-tissue region, is set to 0 (black). This process allows subsequent identification of radiodense regions in the image by concentrating on the tissue region only.

4.3.1 Generation of the Segmentation Mask

A line-scan of a single row in the digitized mammogram is shown in Figure 4.4. The goal is to identify the gray-level transition at the boundary of the tissue region. Note that this line-scan exhibits both local and global variations in gray-level. The global variation corresponds to the transition in the x-ray from the tissue to the non-tissue region, which is often obscured by the local variations corresponding to local changes in tissue density. The large variance of the local variations makes it impossible for a preset threshold to identify the tissue region (the left half of the scan). Furthermore, these local variations within the tissue region also make it very difficult to employ standard edge detection algorithms. A discrete wavelet transform (DWT) based multiresolution

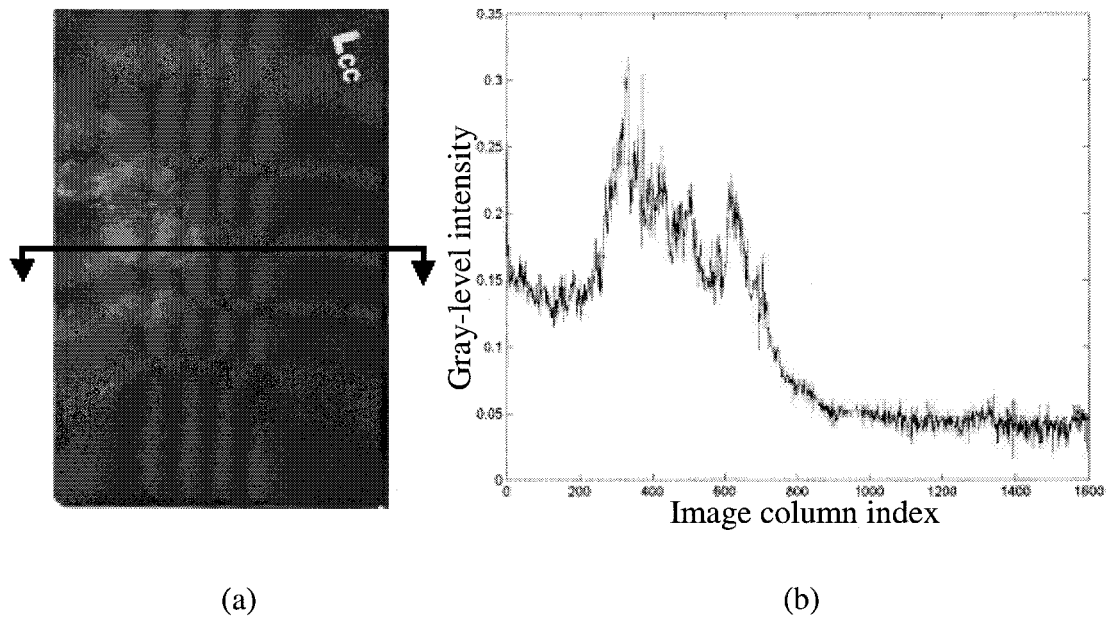


FIGURE 4.4 - (a) Original mammogram image and (b) line-scan of single row of the image as indicated by the line placed on the original image.

decomposition [40] is used to simultaneously model both these variations in the gray-level for each line-scan in the original X-ray image. A polynomial fit is then used to correlate adjacent line scans to generate the final mask template. Figure 4.5 (a) shows a typical image and 4.5 (b) shows the associated automatically created segmentation mask.

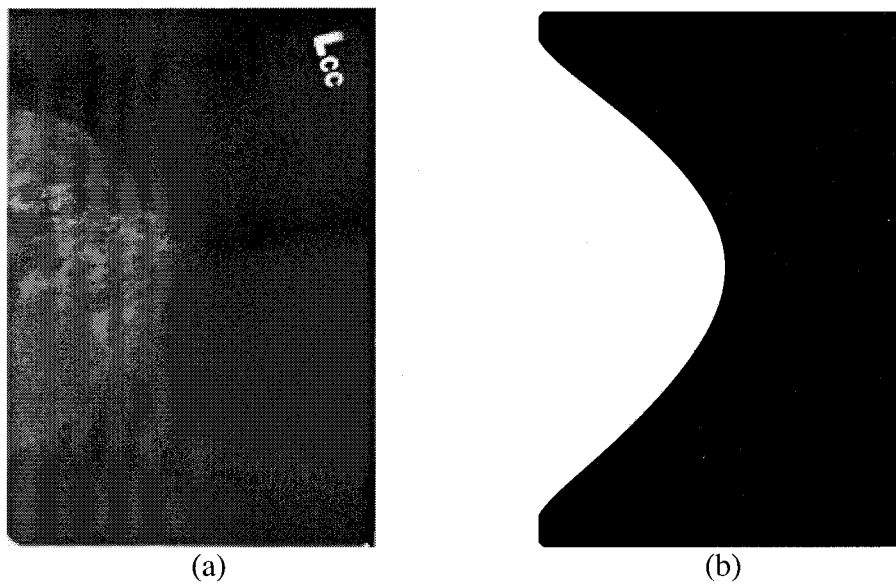


FIGURE 4.5 – (a) Typical image and (b) automatically created segmentation mask.

4.3.1.1 Discrete Wavelet Transform

The DWT is used for modeling local variations and global variations simultaneously in the line-scan, thereby identifying the transition from the tissue to non-tissue region. In particular, the approximation coefficients of each line scan at a particular decomposition level were used to remove the local variations, while conserving the global variations. An extensive study of the image heuristics revealed that the *Daubechies* mother wavelet with five vanishing moments provided the most optimal model. The fifth level approximation coefficients of the original signal provided the space-frequency information corresponding to the tissue boundary of the mammogram. This model is indicated by

$$\begin{aligned} Y_{id}(k) &= \sum_n Y_{(i-1)a}(n) \cdot g(2k-n) \\ Y_{ia}(k) &= \sum_n Y_{(i-1)a}(n) \cdot h(2k-n) \end{aligned} \quad (4.1)$$

where Y_{ia} and Y_{id} are the approximation and detail (DWT) coefficients at the i^{th} level, respectively, and $h(n)$ and $g(n)$ are lowpass and highpass filters, obtained from Daubechies scaling and wavelet functions, respectively. At level zero, Y_{0a} represents the original raw line scan obtained from the image. Figure 4.6 shows the associated wavelet decomposition tree for this system. Figure 4.7 illustrates a typical line scan and the corresponding 5th level approximation coefficients. From these coefficients, a threshold can be easily computed based on the statistical properties of the signal for identifying the tissue boundary.

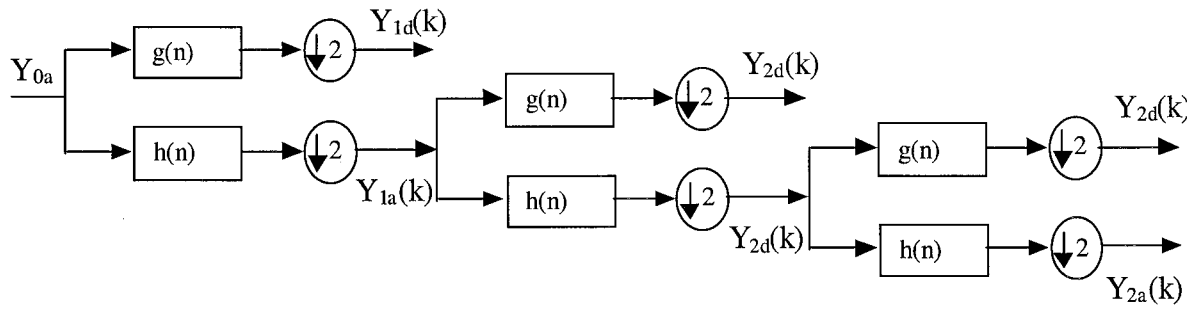


FIGURE 4.6 - Multiresolution wavelet decomposition tree.

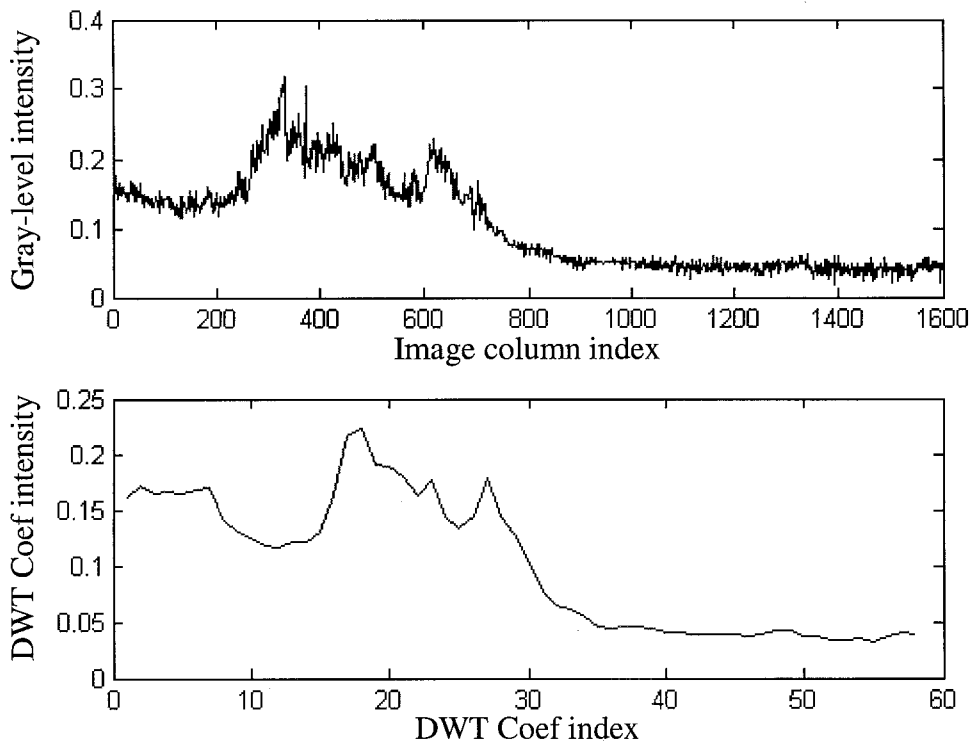


FIGURE 4.7 - A typical line-scan and corresponding 5th level DWT approximation coefficients.

4.4 Tissue Segmentation

The mask generated using the algorithm described above is a binary matrix equal to the size of the original image. Using the above technique the mask matrix is set to a value of 1 (white) in all tissue regions and 0 (black) in all non-tissue regions. We then multiply the corresponding elements in each array using

$$R_{ij} = O_{ij} * S_{ij}; \quad i=1 \text{ to } m, j = 1 \text{ to } n \quad (4.2)$$

where O is the original image and S is the segmentation mask, yields the matrix R . The resulting matrix R is of equal size to O and P and contains the original gray-levels of O in all regions designated by S as being of a tissue region and contains a gray-level value of 0 (black) in all regions designated by S as being a non-tissue region. Results for a typical test image are shown in Figure 4.8.

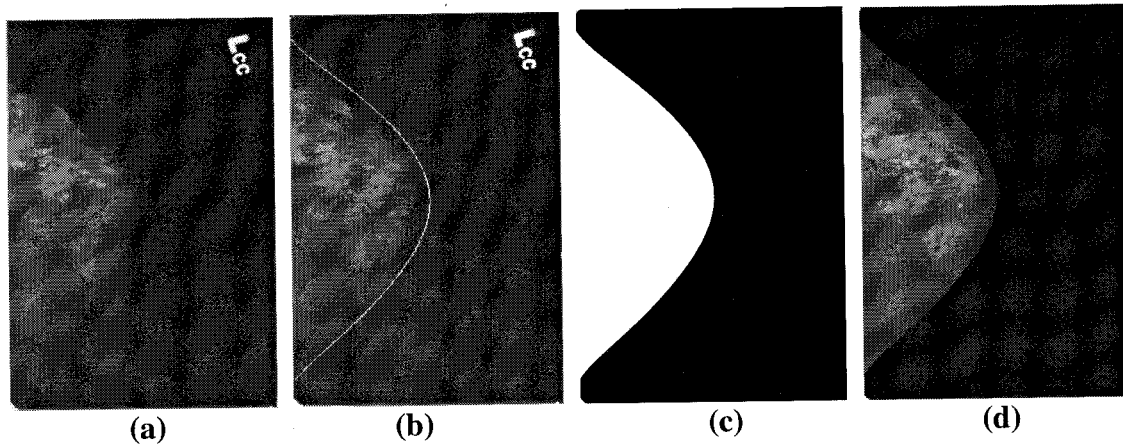


FIGURE 4.8 - Tissue segmentation results for a typical image – (a) original X-ray (b) boundary estimation (c) mask generation (d) tissue segmented image.

4.5 Threshold Determination

Determination of the estimated threshold relies on assumptions made about the images under test. The following assumptions are made in developing the density estimation algorithms:

- a) Pixel gray-level is considered as a deciding factor in segmenting radiodense tissue from radiolucent tissue regions.
- b) The location and shape of the segmented tissue in the mammogram are ignored.

Identifying the radiodense tissue region in a segmented gray-level mammogram image essentially involves converting the 256 gray-level images to binary (black-and-white) format. Radiodense tissue pixels will be assigned a gray-level value of 1 (white) and all other pixels will be 0 (black). However, determining an appropriate gray-level threshold for the conversion process is a non-trivial task. This process is non-trivial because the threshold cannot be an absolute value, but must respond to variations in signal intensity from image to image and local variations within the same image.

Several techniques for generating a dynamic threshold for detecting radiodense indications have been developed. A two-step process is employed:

Step 1: Generate mathematical models of the mammogram image by studying the statistics of the gray-level variations.

Step 2: Apply hypotheses testing (detection theory) techniques for segmenting radiodense and radiolucent pixels.

Details of these steps are provided below.

4.5.1 Image Modeling

The digitized mammogram image is modeled as a stationary Gaussian random field, as described in Chapter 3, using the equation

$$f(x, y) = m_f + \sigma_f w(x, y) \quad (4.3)$$

where $f(x, y)$ is the gray-level value in the mammogram image at location (x, y) , m_f and σ_f are the local mean and standard deviation of $f(x, y)$ and $w(x, y)$ is a zero-mean, unit variance, Gaussian random field. Empirical evidence suggests that such a model is reasonable for typical images [31].

The original image is subdivided into 8×8 blocks; the local mean and standard deviation for the gray-levels are estimated for these blocks. The Gaussian field is synthesized using a pseudo-random number generator and the mammogram image model is created. This model is completely mathematically tractable and can be used for subsequent processing in place of the original image. Figure 4.9 shows a typical image model result – it can be seen that the Gaussian random model is a good replica of the original image.

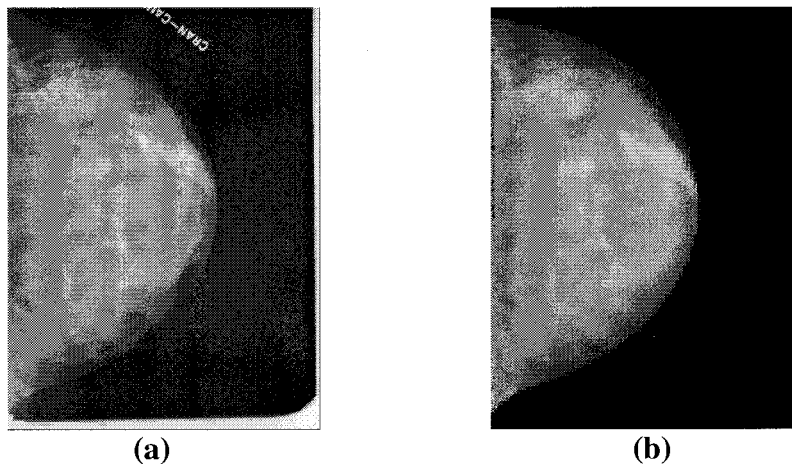


FIGURE 4.9 – (a) Original mammogram image and (b) its Gaussian random model. Note that the segmentation mask has been applied to (b) using the techniques described earlier.

4.5.2 Radiodense Tissue Segmentation

Since the mammogram image has been successfully modeled as a Gaussian random field using its gray-level statistics, we can recast radiodense tissue segmentation as a problem in hypothesis testing (also known as detection theory). In a detection problem, an observation of a random variable is used to make decisions about a finite number of outcomes [32]. In this case, the pixel gray-level under consideration, $f(x, y)$, is the random variable, and the two possible outcomes for that gray-level are radiodense or radiolucent. This two-class situation is also known as binary hypothesis testing. To test the hypothesis, the value of the random variable (pixel gray-level) is compared with a threshold. This threshold is dynamically generated, taking into account the variation in gray-level statistics from image to image and the local statistics within each image.

A variety of algorithms for determining a dynamic threshold for radiodense tissue segmentation have been explored. Segmentation algorithms using four techniques are presented – one classical, and the other three developed specifically for this study.

4.5.2.1 Image segmentation by modeling the threshold as a random variable

This algorithm was developed using data from the FCCC study. Subsequent validation data resulted in a reevaluation of the algorithm. Methods developed for this technique are used in the later final algorithm. This technique was originally presented in [41, 42].

A dynamic threshold for segmentation of the radiodense tissue inside the mammogram film, is described by the equation

$$T_{\text{global}} = T_{\text{nominal}} + \alpha (T_{\text{local}} - T_{\text{nominal}}) \quad (4.4)$$

where T_{local} represents the local gray-level variations, $T_{nominal}$ represents the random image model, α is a parametric weight parameter and T_{global} is the global threshold. If the mammogram were a zero-mean Gaussian random image then

$$T_{global} = T_{local} = T_{nominal} = 50\%. \quad (4.5)$$

since this is a real image, then T_{local} must be determined. To do this, the segmentation threshold is varied across the entire gray scale range. The image is converted to a binary matrix with all pixels above the threshold being set to 1 (white) and all pixels below the threshold being set to 0 (black). The effect of varying segmentation threshold on the percentage of black pixels in a gray-level mammogram image is shown in Figure 4.10

(a). This plot resembles the cumulative distribution function (CDF) of a Gaussian random variable. The probability density function (PDF) can be calculated by differentiating the CDF as shown in Figure 4.10 (b). The mean value of the random variable can be calculated using the PDF. This mean is the local segmentation threshold, T_{local} . The parameter, α , allows the equation to be tuned using a single variable. Implementation of

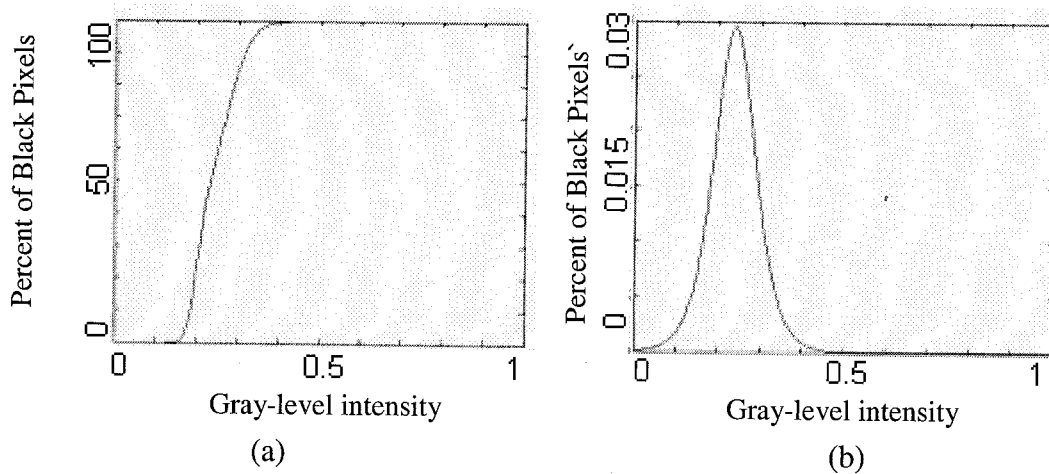


FIGURE 4.10 - (a) Effect of varying segmentation threshold on the percentage of black pixels in a gray-level mammogram image and (b) Probability density function of the threshold random variable.

this technique will involve the determination of α . The resulting segmentation threshold, T_{global} , is used to segment the radiodense tissue.

4.5.2.2 Bayesian segmentation Approach

Baye's decision criterion states that given two distributions that are Gaussian in nature, with equal variance but different means, classification of data can be performed using the following minimum distance function:

$$T_B = \frac{\mu_1 + \mu_2}{2} \quad (4.6)$$

where T_B is the segmentation threshold, μ_1 and μ_2 are the means of the first (radiolucent) and second (radiodense) distributions respectively. Each pixel gray-level value, $f(x, y)$, is compared with the Bayesian threshold, T_B . If $f(x, y)$ is greater than T_B , the pixel is determined to be radiodense. For this algorithm to be successful, it is essential to obtain accurate estimates of the mean values of the two kinds of pixels. Also, the algorithm assumes equal variances (data densities) in the two regions – the latter assumption is not always valid.

4.5.2.3 Augmented Bayesian Segmentation Approach

Analysis of the Bayesian threshold described in the previous paragraph resulted in absolute radiodensity estimates that were unusually high. This result could be either due to incorrect estimates of image region statistics or the fact that a Bayesian threshold is set very low. In the Bayesian approach, the emphasis is on minimizing an average loss

function. Augmenting the Bayesian threshold with a fixed percentage of the original value, using the following equation, increases the threshold:

$$T_{AB} = T_B + pT_B \quad (4.7)$$

where T_{AB} is the augmented Bayesian threshold, T_B is the Bayesian threshold determined using (4.6) and p is a fixed percentage from 0 – 100%. It should be noted that this algorithm, like the strict Bayesian classifier, assumes that the variances of the radiodense and radiolucent pixels are identical.

4.5.2.4 Constrained Neyman-Pearson Segmentation Approach

A constrained version of the Neyman-Pearson function has been developed. This algorithm is based on the heuristics of the cohort of images provided for analysis. Analysis of these images by a strict Bayesian classifier yielded consistent results in rank but provided non-ideal percentage calculations. To overcome this issue a constrained algorithm has been developed that biases the Bayesian classifier based on the local variance of the image and the means of the Gaussian distributions that model the radiodense and radiolucent tissue. The segmentation threshold is now given by the equation:

$$T_{CNP} = \frac{\mu_1 + \mu_2}{2} + \left(\frac{\alpha - \sigma^2}{\alpha} \right) \left(\frac{\mu_2 - \mu_1}{2} \right) \quad (4.8)$$

where T_{CNP} is the constrained Neyman-Pearson threshold, α is a scaling parameter, σ^2 the local variance of the image and μ_1 and μ_2 are the means of the radiolucent and radiodense regions respectively. If α is chosen such that $\sigma_{max}^2 \leq \alpha$, then the bias will constrain the algorithm to values between the Bayesian classifier output and μ_2 . Image heuristics

showed that this bias range would be sufficient to model the threshold of the radiodense tissue region. As the variance of the image approaches α , the term in the first parenthesis tends towards zero and the threshold approaches that of a pure Bayesian classifier. As the variance of the image decreases, the amount of bias increases. As the variance approaches zero, the threshold will move towards the mean of the radiodense tissue region, μ_2 .

4.6 Density Estimation and Image Post-processing

Using T_{global} the image is segmented into a binary matrix. All gray-level values that lie above T_{global} are set to “1” (white) and all other values are set to “0” (black). Using this new binary matrix and the segmentation mask matrix the percentage of radiodense tissue can be determine using

$$\%RadiodenseTissue = \frac{P_{white}}{P_{total} - P_{film}} \times 100\% \quad (4.9)$$

where P_{white} is the total number of white pixels in the matrix, P_{total} is the total number of pixels in the matrix and P_{film} is the total number of pixels in the film-only region, as found using the segmentation mask.

Using the methods proposed in this chapter, a set of images was analyzed. These images were from two separate data sets. The first was provided by FCCC from their Family Risk Analysis Program (FRAP) database. Harvard Medical School provided the second set of ten images for validation purposes. These validation images were previously analyzed using the established “Toronto” method. Chapter 5 presents a collection of the results achieved by applying the algorithms proposed in this thesis on the two sets of images described above.

CHAPTER 5: RESULTS

5.1 Introduction

Dr. Celia Byrne of the Channing Laboratory, Brigham and Women's Hospital, Harvard School of Medicine provided the second set of data. This set consisted of ten images drawn from hospitals across the country. These images are gray-scale scans of mammogram x-rays and have been used for validating the algorithm proposed in this thesis. It is assumed that the images are uncompressed and have not been enhanced or adjusted in any manner after acquisition from the film scanner. Each of the raw images is of a different patient and contains different image characteristics.

These images were initially provided to Rowan University without radiodense percentages. A blind ranking was made in an attempt to show the abilities of the algorithms. Following the blind study, Dr. Byrne provided the radiodensity estimates obtained for each of the images using the "Toronto" method. As described in Chapter 3, this method requires significant knowledge on the part of the radiologist. Although the percentage of radiodense tissue for each image was provided, however, no gray-level thresholds or pixel classifications were included.

5.2 Mask Generation and Tissue Segmentation Techniques

Figure 5.1 shows typical segmentation results obtained by implementing the DWT tissue segmentation technique described in the previous chapter. The images shown in Figure 5.1 indicate that the DWT is able to model the edge of the tissue region with sufficient accuracy. Comparing the dynamically generated mask to a segmentation mask that is generated manually allows for a quantitative analysis of the proximity of the mask

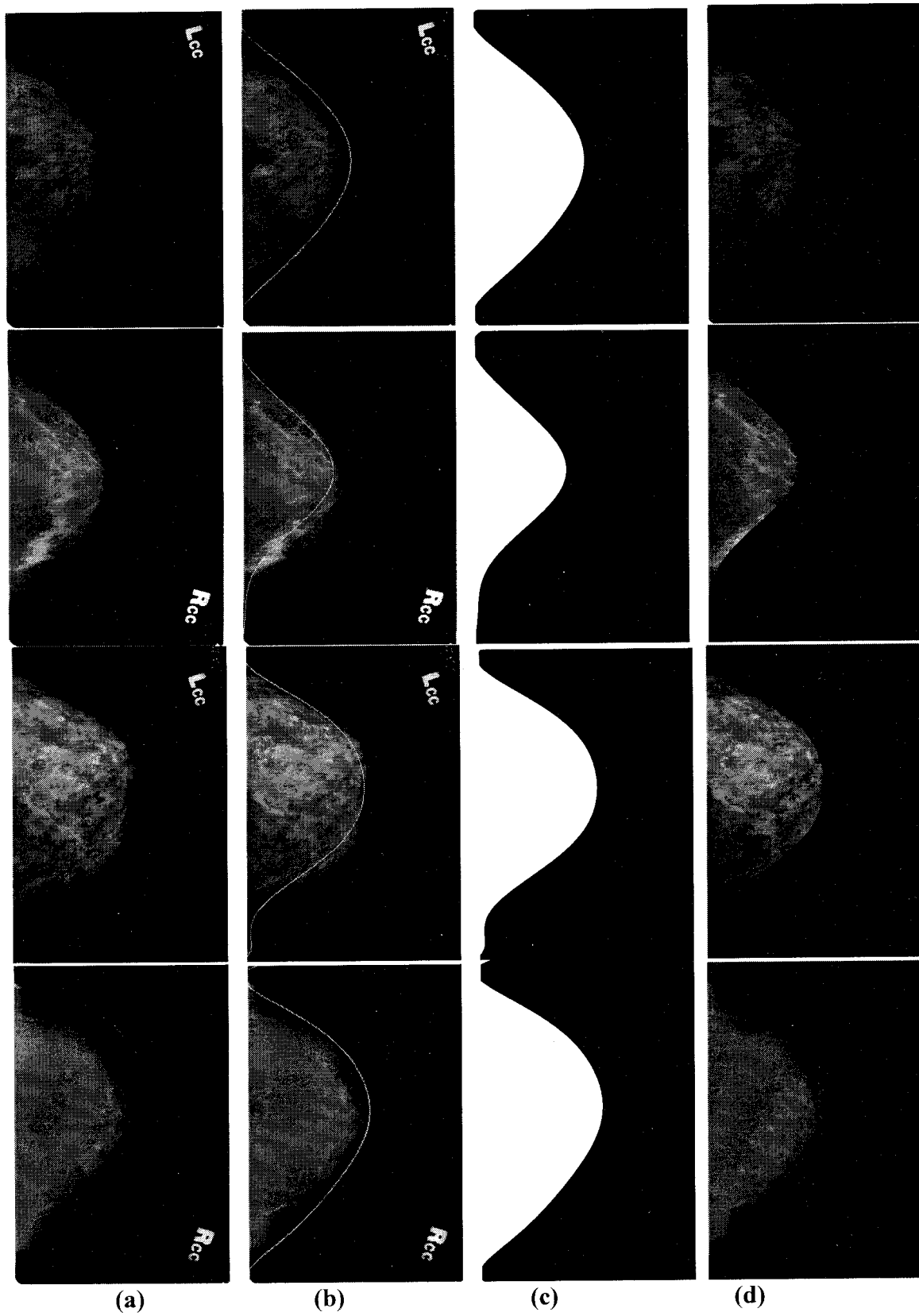


FIGURE 5.1 - Four sets of data showing (a) the original image, (b) edge of tissue region, (c) associated mask and (d) image and mask combined.

contour to the tissue-film boundary. The percentage difference and mean squared error (MSE) as calculated using

$$\%Diff = \left| \frac{(M_{dyn} - M_{man})}{M_{man}} \right| * 100 \quad (5.1)$$

and

$$MSE = \frac{1}{N} \sum |(M_{man} - M_{dyn})|^2 \quad (5.2)$$

where M_{dyn} and M_{man} are the number of 1 (white) pixels in the DWT based segmentation mask and the manually generated mask, respectively, and N is the total number of pixels in the image.

Table 5.1 lists the percentage difference and MSE for each of the four images shown in Figure 5.1. It should be noted that the manual segmentation mask is assumed to provide the exact tissue boundary. Therefore all error figures are compared with respect to this benchmark. However, often times in image processing applications, the true

TABLE 5.1 - Percentage and mean squared error from manually developed reference mask for patients from figure 5.1.

Patient ID	View	M_{man}, Manual Mask (pixels)	M_{dyn}, Dynamic Mask (pixels)	% diff	MSE (x10⁴)
1	lcc	829614	1049359	26.48	1.1641
2	rcc	861665	653900	24.11	1.1507
3	lcc	1197724	988142	17.49	1.2789
4	rcc	1049230	1216404	15.93	0.7431

performance of the algorithm can only be assessed by subjective visual evaluation of the resulting image. Furthermore, the MSE is only meaningful for relative comparison of different masks. With that in mind the numbers given in Table 5.1 should be interpreted within these guidelines.

5.3 Radiodense Tissue Segmentation Algorithms

Four algorithms have been developed for the dynamic segmentation of radiodense tissue in the breast region of a digitized mammogram. The first algorithm was developed and tested using data from the Fox Chase Cancer Center Family Risk Analysis (FRAP) program. After development of this initial algorithm, validation data from Dr. Byrne was provided. Based on the heuristics of the validation data, and the subsequently provided radiodense tissue percentages, several algorithms were developed and exercised. The following sections present results obtained from this portion of the research.

5.3.1 Image segmentation by modeling the threshold as a random variable

The heuristics of this data showed strong low intensity characteristics and little information in the higher intensity regions. Figure 5.2 shows the gray-level histogram of a typical image from the FCCC dataset. It can be seen from the figure that there is little information contained in the higher intensity regions. Equation 4.4 was developed using this characteristic as a basis. The scaling parameter, α , allows for fine-tuning of the dynamic threshold generated using the algorithm. Table 5.2 shows the estimated radiodense tissue percentages resulting from exercising the algorithm for three patients using varying values of alpha. Figure 5.3 shows the resulting segmented tissue.

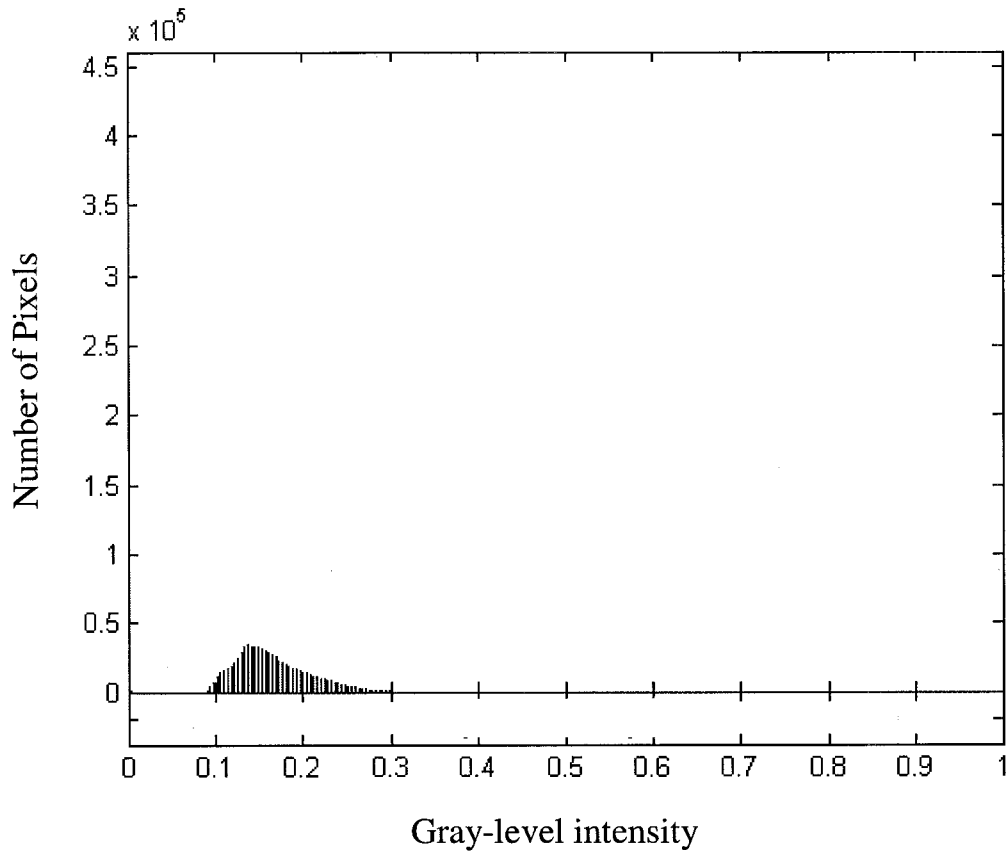
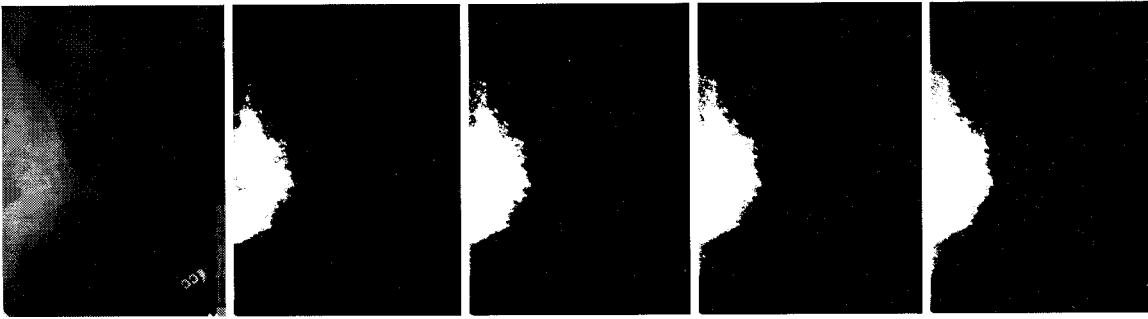


FIGURE 5.2 – Histogram of tissue region of typical image from the FCCC dataset

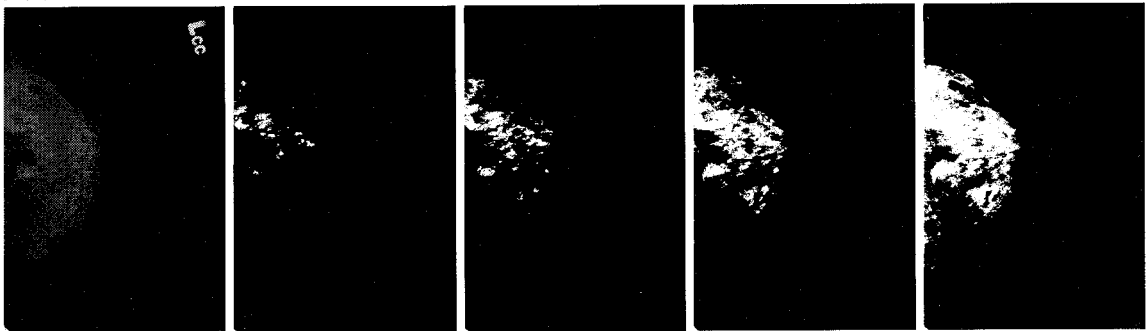
TABLE 5.2 - Summary of percentages of radiodense tissue for patients from Figure 5.3.

Patient Number	α , scaling parameter			
	0.65	0.75	0.85	0.95
1	33.95 %	37.50 %	41.96 %	45.67 %
2	2.69 %	7.76 %	19.11 %	37.31 %
3	13.86 %	23.15 %	40.23 %	55.04 %

Patient 1



Patient 2



Patient 3

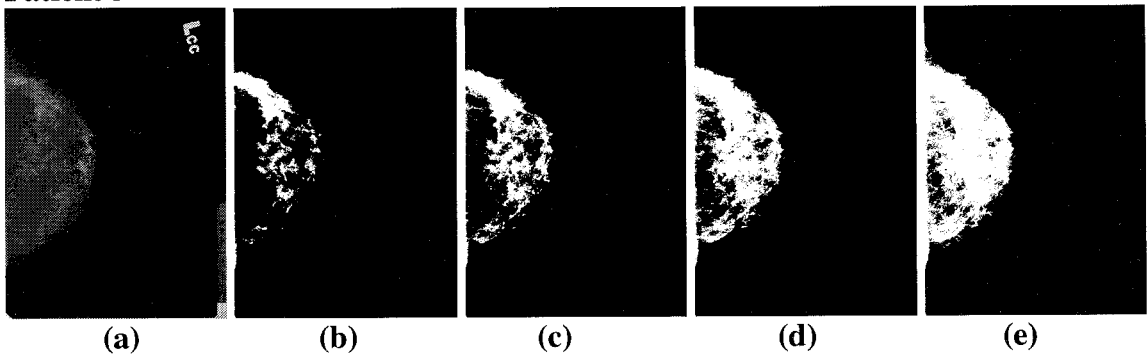


FIGURE 5.3 - Typical results showing (a) the original image and (b-e) the binary segmented tissue region resulting from $\alpha = 0.65, 0.75, 0.85, 0.95$ respectively for three patients.

In order to validate the algorithm, images were needed with known radiodense tissue percentages. While in the developmental stages of this technique, several meetings with Dr. Cathy Evers, Head Radiologist at FCCC, indicated promise in the proposed technique although final validation was required.

5.3.2 Algorithm modification based on validation data

As stated, ten images were provided for validation purposes. The images provided by Dr. Byrne are bitmap formatted files rather than mammogram film. Upon inspection of the images it can easily be seen that the heuristics of the validation images are different from those used to develop the algorithm outlined in Section 5.3.1. Comparing Figure 5.2 with Figure 5.4 reveals this difference. The main difference between the two sets of images is the intensity distribution. This is most likely due to scanning conditions and the quality of the equipment used to digitize the x-ray film.

Dr. Byrne's assistance in validation required that first a blind classification of the

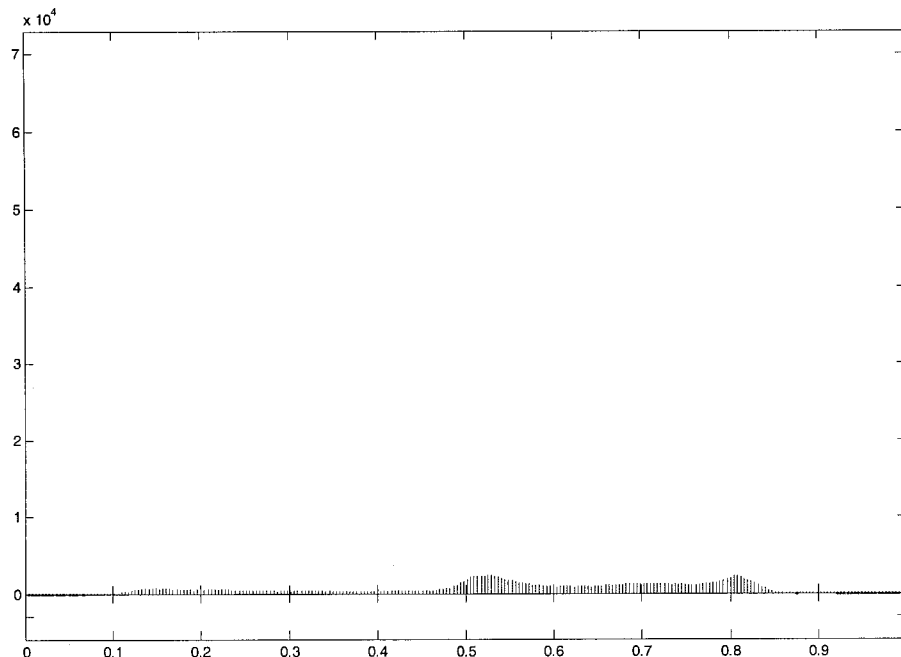


FIGURE 5.4 – Histogram of an image provided by Dr. Celia Byrne. Comparison to figure 5.2 reveals the differences in the tow datasets intensity values.

validation data be made to test the algorithms raw abilities. It was expected that the algorithm would be able to rank the images with a certain amount of accuracy. The following sub-sections describe the procedure for implementing the blind classification and the final implementation of the supervised classification using the rank and radiodense percentage data that was eventually provided.

5.3.2.1 Blind classification

Blind training refers to implementing an algorithm without using some sort of baseline data. The baseline data has known results that allow proper gauging of the algorithms performance. Not having this data meant that all of the parameters for implementation of the algorithms needed to be established without expert knowledge. The method of blind classification is common in the medical research where proper operation can easily be gauged. In the engineering research of medical imaging, and imaging processing in general, researchers prefer to have a baseline dataset to train their algorithms and measure performance. This baseline data is often from established techniques. In the case of medical image processing it is often provided by medical researchers.

5.3.2.1.1 Initial threshold determination

Because the basis for all of the presented algorithms is the Bayesian classifier, proper performance requires knowledge of the underlying distributions. In order to establish this baseline a threshold was chosen for each image arbitrarily. These initial thresholds were chosen to segment the images approximately using cues that could be

inferred from manual inspection. The mean of each segmented region is calculated along with the variance.

5.3.2.1.2 Initial determination of scaling parameters

Using the estimations described above the scaling parameters for the algorithms were set to segment the images in a manner that provided a ranking consistent with visual inspection.

5.3.2.1.3 Results

These blind segmentation results were presented to Dr. Byrne as only a ranked set. The images were ranked from 1 to 10, with 1 corresponding to least radiodense and 10 corresponding to most radiodense. It was easily foreseeable that the predicted percentages determined by the algorithm would be incorrect since no data was given as a baseline. It was hoped that the blind ranking of the images would be fairly accurate when analyzed against the radiologist percentage ranking. The results were analyzed by Dr. Byrne after which she provided the known ranking of the images and her expertly determined percentage of radiodense tissue for each image. The initial ranking and those provided by Dr. Byrne are given in Table 5.3 below. Analysis showed the strongest correlation between the constrained Neyman-Pearson method, developed specifically for this research, and the radiologist expert results.

TABLE 5.3 – Blind Segmentation Rank using each method and expert rank provided afterwards by Dr. Byrne.

Patient Number	Image rank using various thresholds 1: Least percent radiodense; 10: Most percent radiodense			
	Bayesian, T_B	Augmented Bayesian, T_{AB}	Constrained Neyman-Pearson, T_{CNP}	Expert ranking provided by Dr. Byrne
11051709	2	4	4	5
11599502	6	5	3	3
14480101	8	8	10	8
15839502	3	1	5	4
19131709	10	10	9	1
20110811	7	2	1	2
26253102	1	3	2	6
26799401	5	7	6	10
27786202	4	6	7	9
28657701	9	9	8	7

5.3.2.2 Supervised classification

Analysis of the ranked data provided by Dr. Byrne revealed that the Constrained Neyman-Pearson algorithm had the closest correlation to the expert ranking. The constrained Neyman-Pearson algorithm that has been presented allows for the dynamic determination of a threshold value between the pure Bayesian classifier,

$$T_B = \frac{\mu_1 + \mu_2}{2} \quad (5.1)$$

where μ_1 and μ_2 are the means of two known underlying distributions and μ_2 , the greater of the two means. This threshold is dynamically determined based on the scaling parameter, α , and the variance, σ^2 . With knowledge of the radiodense tissue percentage that is present in the validation images, the algorithm could be trained to give not only

well-correlated rank but also accurate radiodense tissue estimations. There are two main hurdles with training the algorithm:

- a) Initial threshold determination for modeling the underlying distributions that allow proper performance of the algorithm.
- b) Determination of the scaling parameter, α , which determines the contribution of the constrained bias portion of the algorithm.

5.3.2.2.1 Automated initial threshold determination

During the blind classification of the algorithm, the underlying distribution was estimated using an arbitrarily chosen threshold as described in Section 5.3.2.1. In order to meet the ultimate goal of automated segmentation of the radiodense regions there needs to be a method for dynamically determining the parameters of the underlying distribution of the image. This was determined using a technique originally published by Neyhart *et al* [41]. It can be shown that the qualitative terms, “bright” and “dark” can be quantified. Given a Gaussian distribution all pixels with an intensity level greater than the mean of the distribution are “bright” and all pixels with intensity levels less than the mean are indeed “dark.” This is illustrated in Figure 5.5.

It was shown that as the gray-level segmentation threshold is varied from 0 to 1 the percentage of radiodense tissue matched the cumulative distribution function (CDF) of a Gaussian random variable. The probability density function (PDF) can then be determined by differentiating the CDF. The mean of the PDF is the point about which the image can be segmented into “bright” and “dark” regions. This is the point that is chosen as the initial threshold. Using this initial threshold as the segmentation point allows for

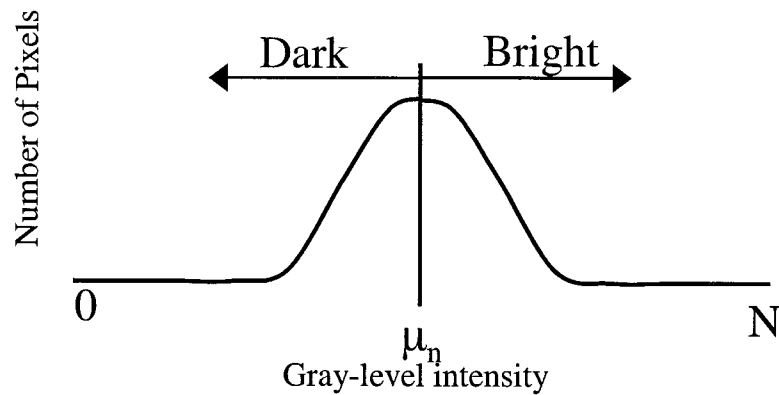


FIGURE 5.5 – Gaussian distribution of pixel intensities showing the regions considered “dark” and “bright.”

the determination of the means and variance of the underlying distributions.

This initial threshold needs to be augmented however. An analysis of the heuristics of the validation images shows that this threshold very rarely segments the radiolucent and radiodense tissue regions. It then becomes evident that the radiodense tissue is not truly the “bright” tissue but a subset of that region containing the brightest portions. Just as the Neyman-Pearson algorithm is able to provide a bias towards one classification the constrained algorithm allows for a bias towards the subset of the “bright” tissue region that contains the radiodense tissue.

5.3.2.2.2 Determination of the scaling parameter, α

The scaling parameter, α , determines where the final threshold lies. The scaling parameter defines the contribution that the constrained portion of the equation gives to the final threshold value. As stated in Section 5.5.2.4, if α is chosen such that $\sigma_{max}^2 \leq \alpha$ then the bias will constrain the algorithm to values between the Bayesian classifier output and μ_2 . This is a fixed value used for all classifications and is set based on image

statistics and the accuracy of the initial threshold.

There are several ways that the value of α can be chosen experimentally. The first method involves a single training data point. Using this method a value for α is chosen so that the percentage of radiodense tissue calculated by the algorithm matches the expertly determined percentage of radiodense tissue. Using this technique the performance of the algorithm is measured against the classification of the remaining nine images. The second method involves minimizing the classification error between n out of the M images provided ($n < M$). In this technique the value of α is chosen so that the smallest classification error exists between the n data points. Performance of the algorithm is measured against the remaining images ($M - n$).

5.3.2.2.3 Results

The assumption is made that the percentages of radiodense tissue provided for validation is based only on a gray-scale threshold. Only percentage values were given for the images. Consequently, the images were analyzed to find the associated threshold. To obtain this threshold each image was segmented to match the given percentage of radiodense tissue with a single gray-level value, T_v . This validation threshold takes on one of 256 values normalized on a 0 to 1 scale and accurately matches the given percentage to within 1% of the actual value (although in most cases much closer than that). Table 5.4 shows the quantitative segmentation results provided by Dr. Byrne and the associated threshold, T_v , resulting from analysis of the image. Figure 5.6 shows the actual percentage of radiodense tissue and the percentage calculated using T_v . This illustrates the accuracy of the matched threshold at segmenting the given percentage of

TABLE 5.4 - Validation Images and associated data; ranked by increasing radiodense percentage.

Image Number	Percentage radiodense of validation data	T_v, threshold of validation data	Expert percentage from using T_v
19131709	1.5	0.801	1.3
20110811	2.5	0.711	2.8
11599502	12.9	0.723	13.4
15839502	13.3	0.696	14.3
11051702	21.4	0.645	21.1
26253102	22.5	0.672	21.6
28657701	33.6	0.801	33.2
14480101	40.8	0.727	41.2
27786202	50.1	0.583	50.6
26799401	55.3	0.551	55.2

tissue from the image.

The validation thresholds, T_v , were used as a baseline goal with which to measure algorithm performance during implementation along with the actual percentages of radiodense tissue. Because of the distribution of pixel intensities in the images, small errors in threshold are capable of creating large differences radiodense tissue percentage. For this reason performance was measured using these two criteria.

Analysis of the images using the initial threshold revealed very unsatisfactory results in both percentage and threshold. Further analysis showed that this was the result of the upper bound of the algorithm, μ_2 , being less than T_v for the images. In order to

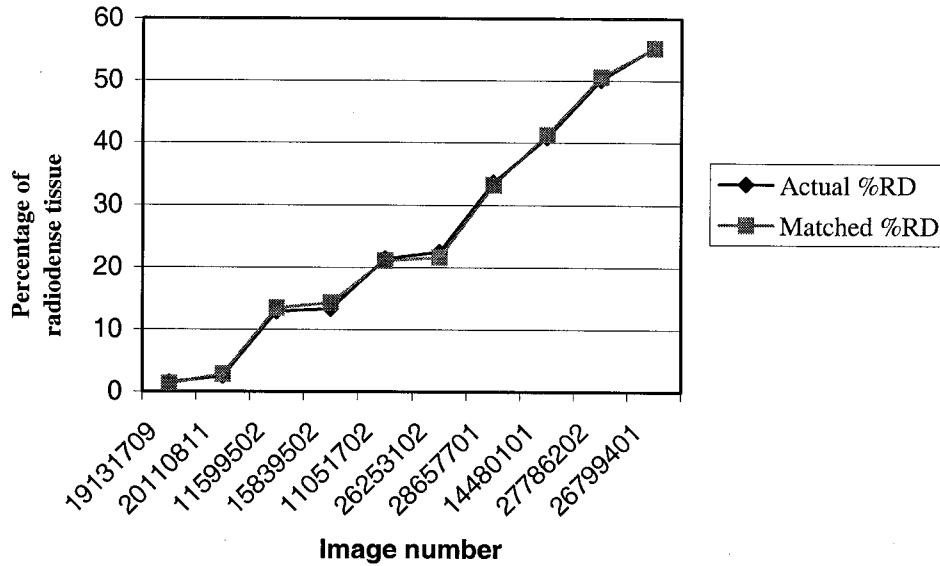


FIGURE 5.6 – Actual percentage of radiodense tissue and percentage of radiodense tissue calculated using the best-matched threshold from Table 5.5.

allow for proper analysis of the images the threshold was augmented by a percentage.

This consequently moved the upper bound of the algorithm, μ_2 , to greater than T_v for the images allowing proper classification.

It was discovered, however, that over the range of images the augmented threshold required to produce minimal classification error changed. It is already known that knowledge of the underlying distributions is essential for proper performance of the proposed method. Based on that knowledge and the observed behavior it can be concluded that, for proper performance to be realized, a great deal of validation data is needed with pixel level classification so that usable results for the underlying distributions can more accurately be modeled.

It can be reasonably concluded that if the data can be classified using different augmented initial thresholds and a single scaling parameter, α , then the algorithm is performing properly. The differences in performance are due to the inability to properly

model the underlying distributions that make up the images. Accordingly the entire set of ten images was classified using a total of three augmented initial thresholds and a single scaling parameter, $\alpha = 0.0025$.

Figures 5.7-5.9 show results obtained from augmenting the initial threshold to 127% of its original value. Figure 5.7 is the segmented images obtained. Figure 5.8 shows the threshold that was calculated as compared to the validation threshold, T_v . Figure 5.9 shows the calculated percentage of radiodense tissue as compared with the known percentages. It can be seen from the graph of Figure 5.9 that this analysis matches the first three images (19131709, 20110811, 11599502) with minimal error.

Figures 5.10 – 5.12 show results obtained from augmenting the threshold to 115% of its original value. Figure 5.10 is the segmented images obtained. Figure 5.11 shows the threshold that was calculated as compared to the validation threshold, T_v . Figure 5.12 shows the calculated percentage of radiodense tissue as compared with the known percentages. It can be seen from the graph of Figure 5.12 that this analysis matches the fourth through seventh images (15839502, 11051702, 26253102, 28657701) with minimal error.

Figures 5.13-5.15 show results obtained from augmenting the threshold to 80% of its original value. Figure 5.13 is the segmented images obtained. Figure 5.14 shows the threshold that was calculated as compared to the validation threshold, T_v . Figure 5.15 shows the calculated percentage of radiodense tissue as compared with the known percentages. It can be seen from the graph of Figure 5.15 that this analysis matches the last two images (27786202, 26799401) with minimal error. Image number 14480101 could not be satisfactorily classified by the algorithm using any of the three techniques.

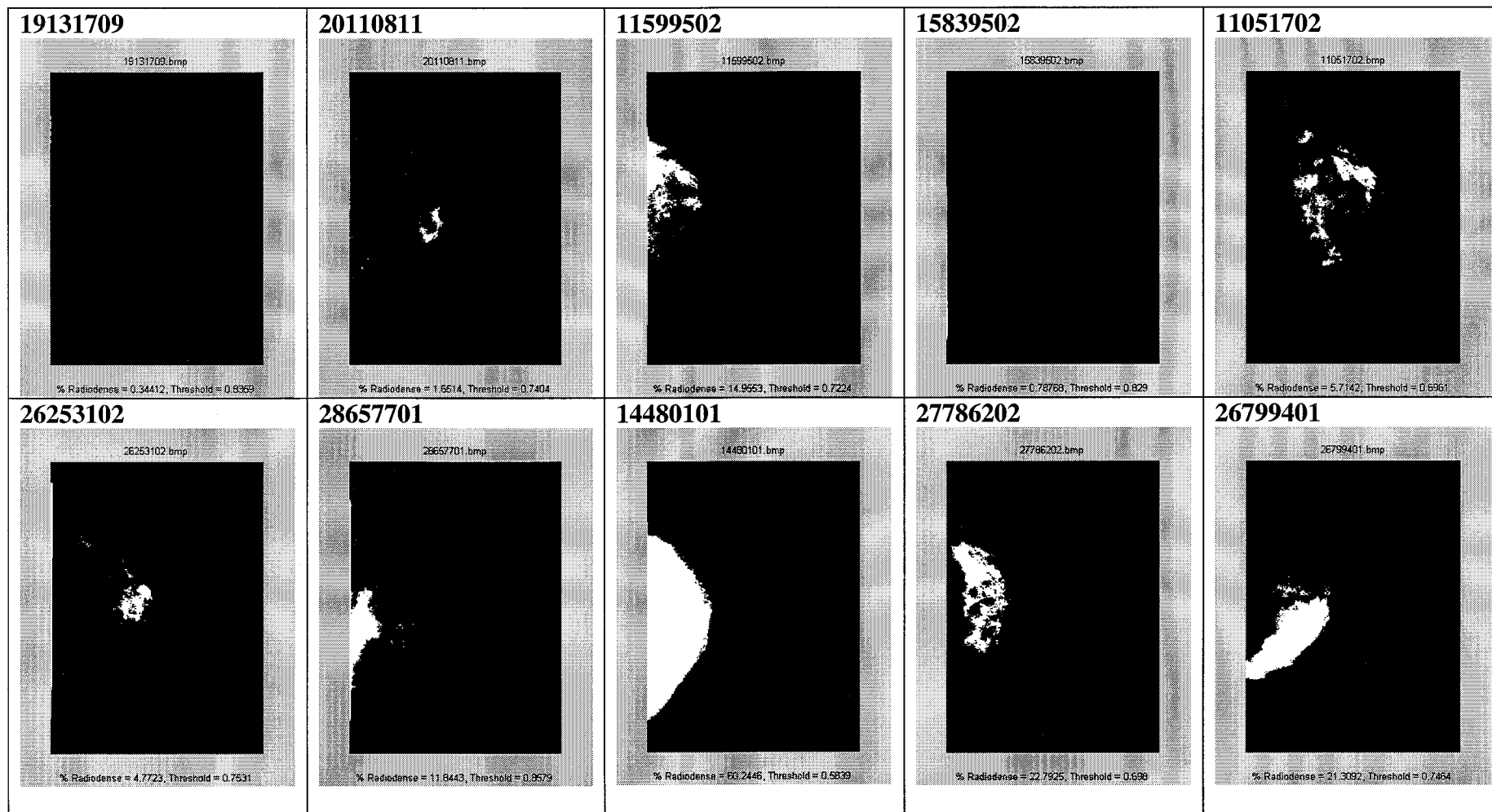


FIGURE 5.7 – Segmented images using 127% of initial threshold. This method segments 19131709, 20110811, 11599502 with minimal classification error.

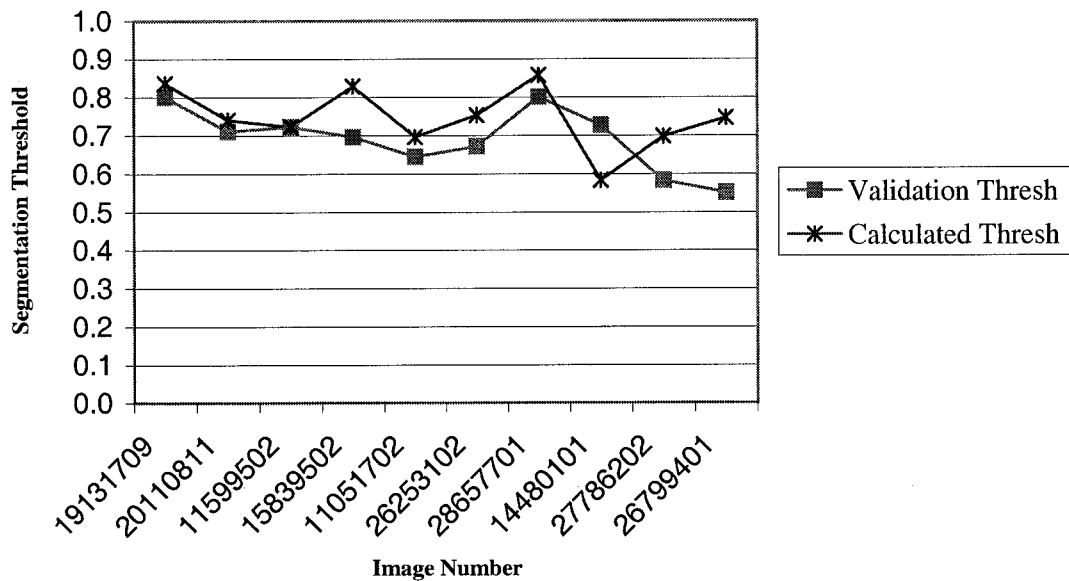


FIGURE 5.8 – Threshold resulting from analysis of image using 127% of initial threshold.

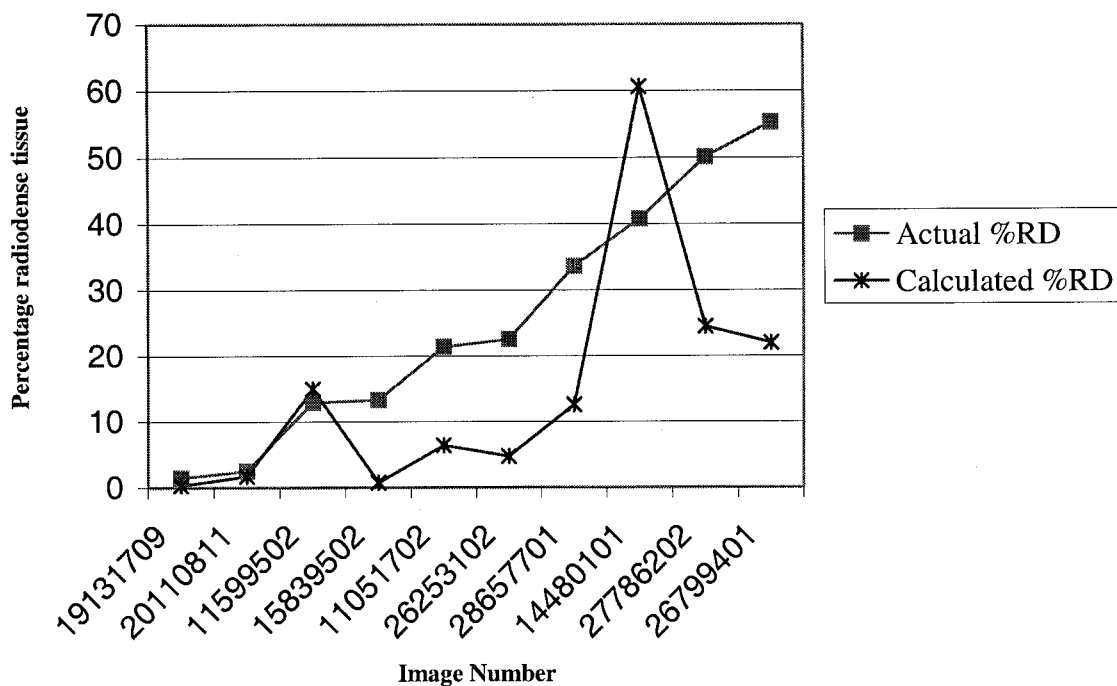


FIGURE 5.9 – Percentage of radiodense tissue resulting from analysis of image using 127% of initial threshold.

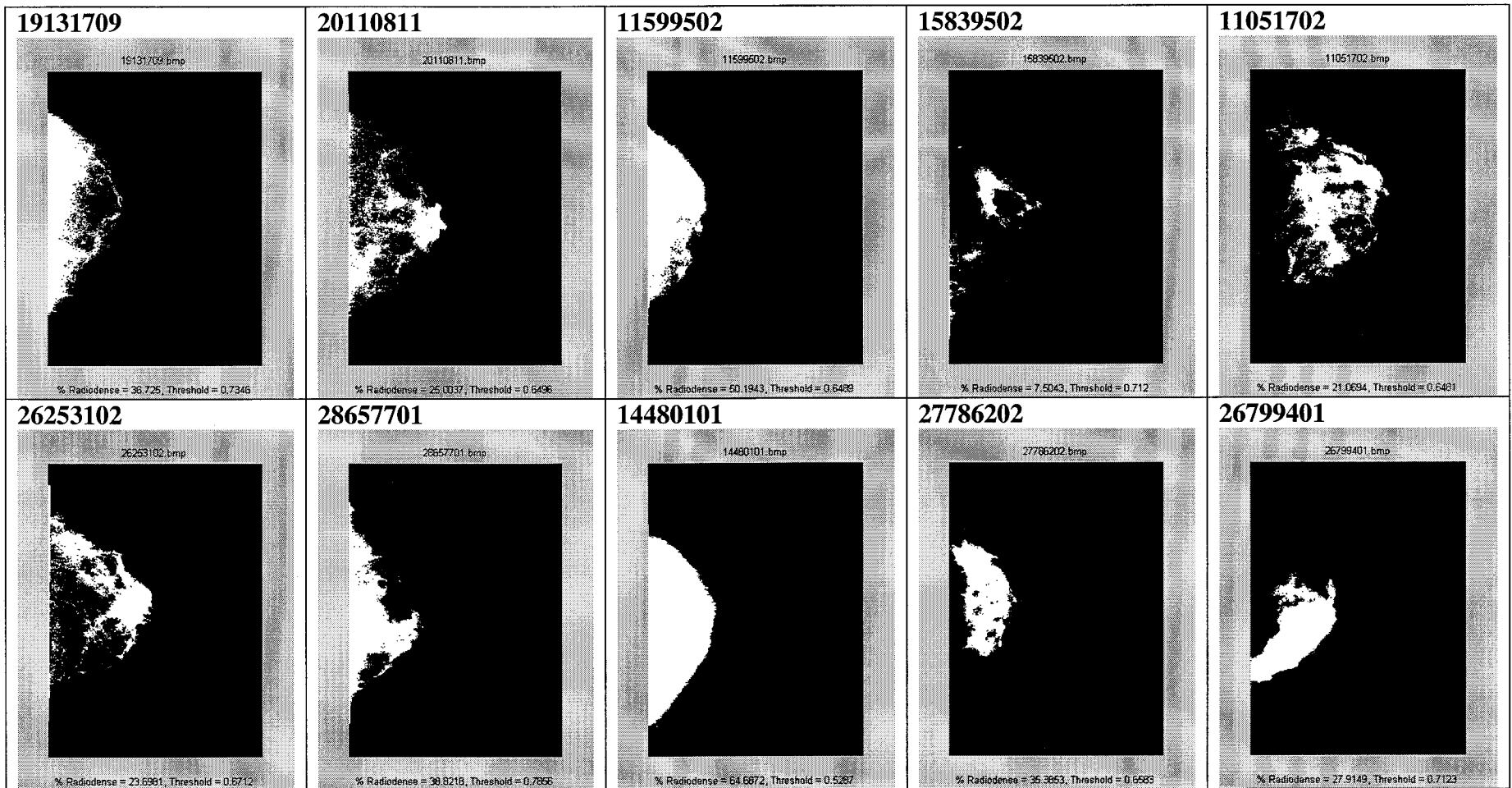


FIGURE 5.10 – Segmented images using 115% of initial threshold. This method segments 15839502, 11051702, 26253102, 28657701 with minimal classification error.

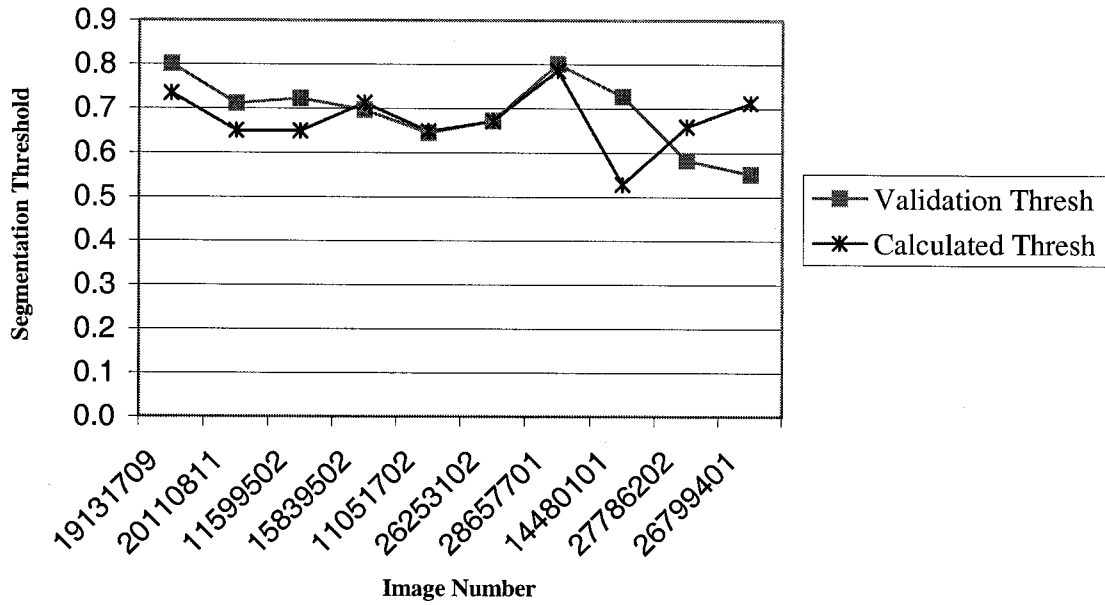


FIGURE 5.11 - Threshold resulting from analysis of image using 115% of initial threshold.

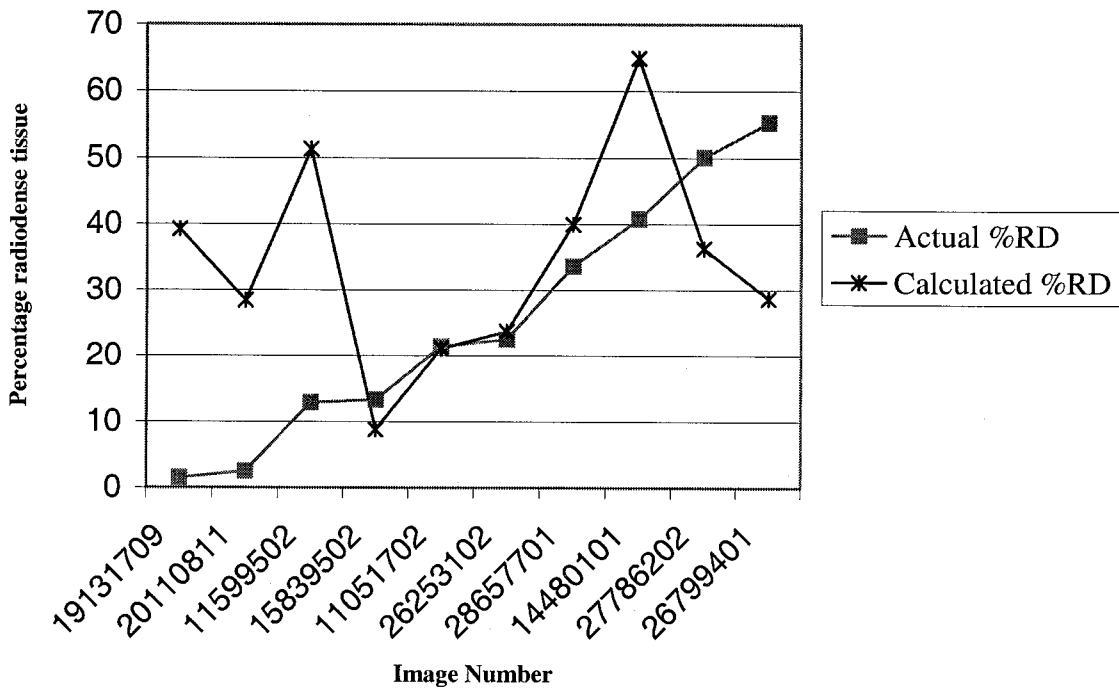


FIGURE 5.12 - Percentage of radiodense tissue resulting from analysis of image using 115% of initial threshold.

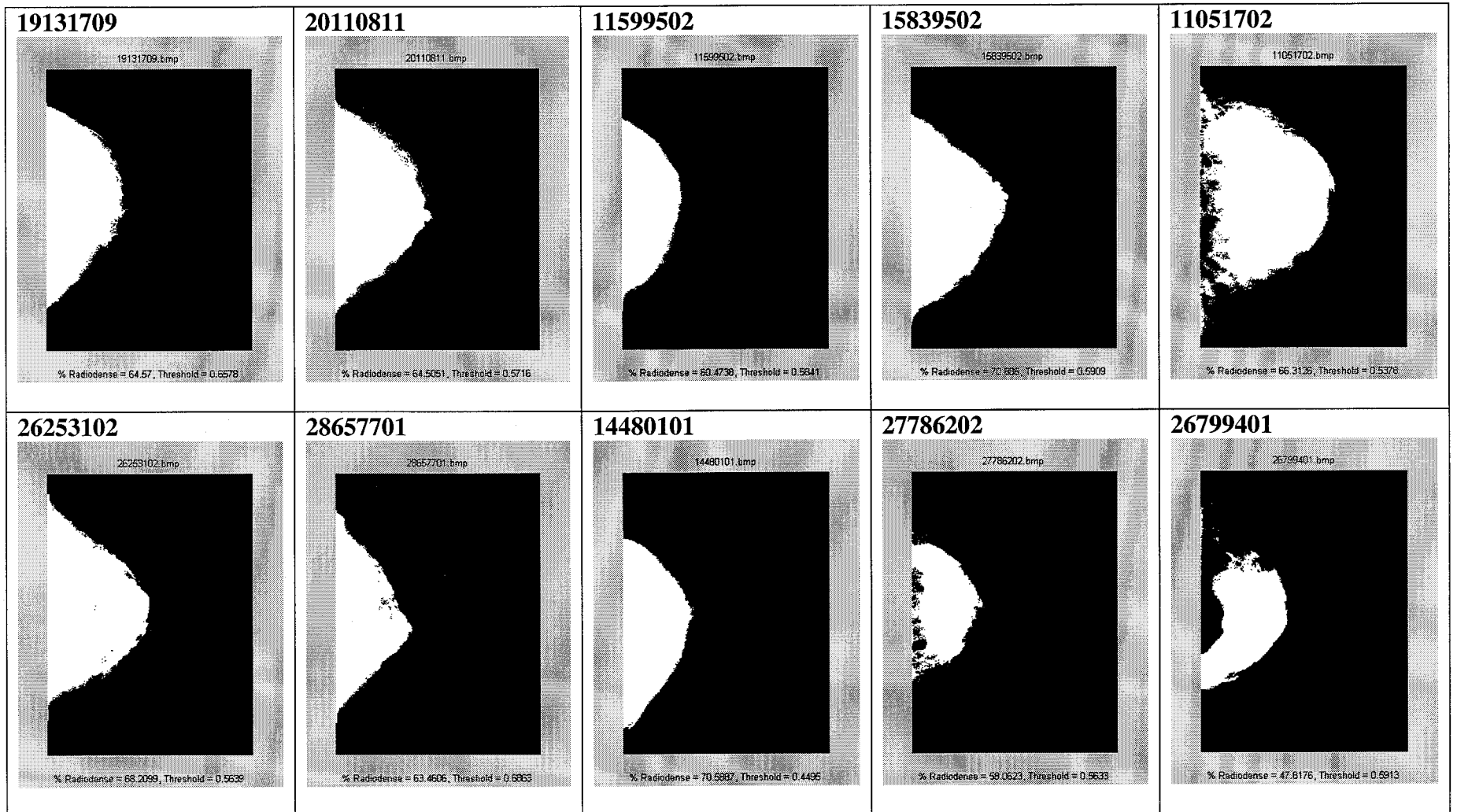


FIGURE 5.13 – Segmented images using 80% of initial threshold. This method segments 27786202 and 26799401 with minimal classification error.

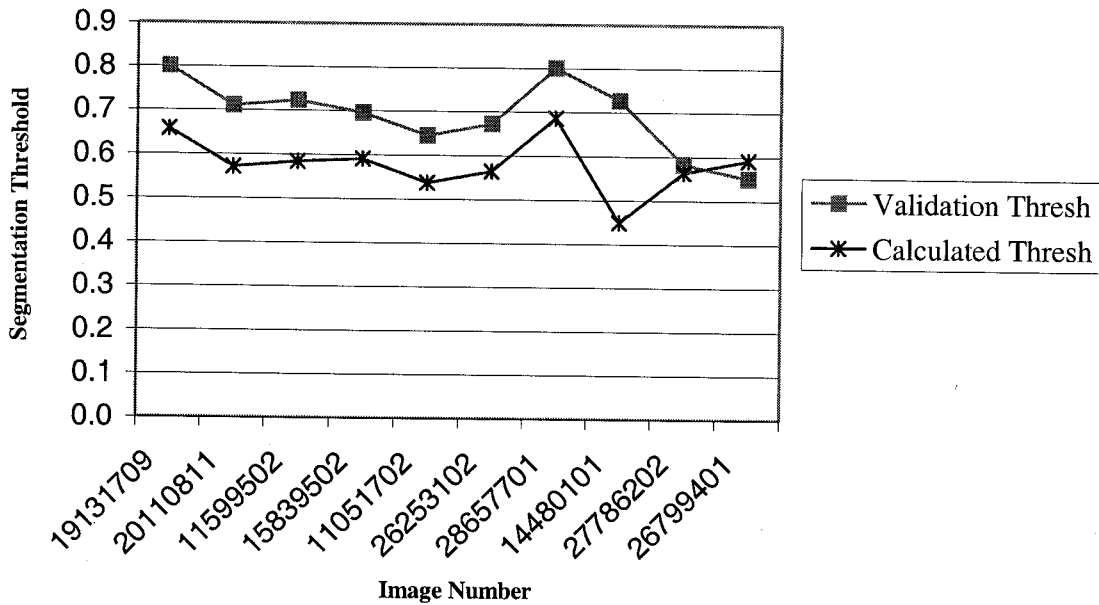


FIGURE 5.14 - Threshold resulting from analysis of image using 80% of initial threshold.

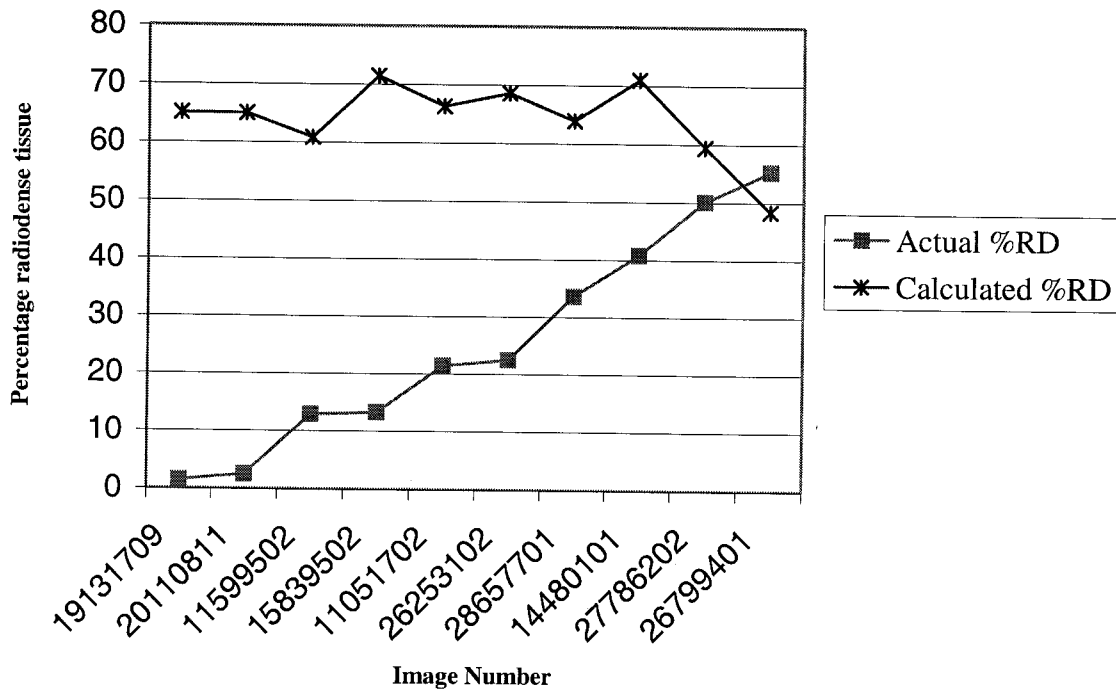


FIGURE 5.15 - Percentage of radiodense tissue resulting from analysis of image using 80% of initial threshold.

Table 5.5 below shows the actual percentage of radiodense tissue given for each image and the calculated percentages for each of the initial thresholds used. The error percentages are given in Table 5.6. Table 5.7 shows the validation threshold, T_v , and the thresholds calculated for each of the initial thresholds used. The error percentages are given in Table 5.8

TABLE 5.5 - Validation threshold, T_v , and the final threshold determined for each initial threshold.

Image Number	Validation threshold, T_v	Threshold for 127% Initial	Threshold for 115% Initial	Threshold for 80% Initial
19131709	0.801	0.8359	0.7346	0.6578
20110811	0.711	0.7404	0.6496	0.5716
11599502	0.723	0.7224	0.6489	0.5841
15839502	0.696	0.8290	0.7120	0.5909
11051702	0.645	0.6961	0.6481	0.5378
26253102	0.672	0.7531	0.6712	0.5639
28657701	0.801	0.8579	0.7856	0.6863
14480101	0.727	0.5839	0.5287	0.4495
27786202	0.583	0.6980	0.6583	0.5633
26799401	0.551	0.7464	0.7123	0.5913

TABLE 5.6 – Percentage error for the final threshold determined for each initial threshold. Uses $|(T_v - T_{CMP})/T_v|*100\%$.

Image Number	Validation threshold, T_v	Percentage error for 127% Initial	Percentage error for 115% Initial	Percentage error for 80% Initial
19131709	0.801	4.3571	8.2896	17.8777
20110811	0.711	4.1350	8.6357	19.6062
11599502	0.723	0.0830	10.2490	19.2116
15839502	0.696	19.1092	2.2989	15.1006
11051702	0.645	7.9225	0.4806	16.6202
26253102	0.672	12.0685	0.1190	16.0863
28657701	0.801	7.1036	1.9226	14.3196
14480101	0.727	19.6836	27.2765	38.1706
27786202	0.583	19.7256	12.9160	3.3791
26799401	0.551	35.4628	29.2740	7.3140

TABLE 5.7 – Provided percentage of radiodense tissue and amount calculated for each initial threshold.

Image Number	Percentage radiodense of validation data	Percentage radiodense of 127% Initial	Percentage radiodense of 115% Initial	Percentage radiodense of 80% Initial	Rank of image based on algorithm classification	Rank of image based on actual classification
19131709	1.5	0.3441	39.2279	65.1	1	1
20110811	2.5	1.7608	28.4430	65.0	2	2
11599502	12.9	14.9553	51.3633	60.9	4	3
15839502	13.3	0.7931	8.8332	71.4	3	4
11051702	21.4	6.4253	21.0694	66.3	5	5
26253102	22.5	4.7723	23.6981	68.6	6	6
28657701	33.6	12.5411	39.9421	63.9	7	7
14480101	40.8	60.6262	64.9368	71.0	10	8
27786202	50.1	24.4514	36.2967	59.5	9	9
26799401	55.3	21.9876	28.6663	48.4	8	10

TABLE 5.8 - Percentage error for the calculated radiodense tissue percentage determined for each initial threshold. Uses $|(T_v - T_{CMP})|$.

Image Number	Percentage radiodense of validation data	Percentage error for 127% Initial	Percentage error for 115% Initial	Percentage error for 80% Initial
19131709	1.5	1.15	37.72	63.62
20110811	2.5	0.73	25.94	62.52
11599502	12.9	2.05	38.46	47.97
15839502	13.3	12.50	4.46	58.13
11051702	21.4	14.97	0.33	44.91
26253102	22.5	17.72	1.19	46.07
28657701	33.6	21.05	6.34	30.31
14480101	40.8	19.82	24.13	30.15
27786202	50.1	25.64	13.80	9.37
26799401	55.3	33.31	26.63	6.89

CHAPTER 6: CONCLUSIONS

Cancer is the second leading cause of death among American women and breast cancer is the second most common form among women. The early detection and treatment of breast cancer is paramount to survival of its victims. Mammography has been established as an inexpensive, non-invasive means of screening for breast cancer. Along with the detection of eminent danger a radiologist must be concerned with the patients future risk of developing breast cancer. The likelihood of a person developing breast cancer at a later date is based on the risk factors that they possess. One such risk factor is the amount and percentage of radiodense tissue in the breast. It has been shown that women with 60-75% breast density are at a four to six fold increase in risk to develop breast cancer.

Trained radiologists working subjectively have traditionally performed breast density measurements. The first system, developed in the mid-1970s, categorized breast density in four broad areas. This system suffered greatly from inter- and intra-observer inconsistencies since it was not based on a quantifiable measure. A revised method was introduced that grouped mammograms into categories of increasing density by percentage. This method allowed for greater quantitative measurement since it is based on a definable scale. This system still required the radiologist to classify the mammogram and, although to a lesser extent, still suffered from the fallbacks of the previous method. More recently computer aided tools have allowed the radiologists to achieve a higher rate of quantitative analysis by allowing them to segment out the breast density, after which the computer program calculates the amount and percentage of the segmented density. This method showed great improvements in consistency both between operators and

within an operator.

An obvious next step is the automation of this process to completely quantify the analysis system. A fully automated system would eliminate inter- and intra-observer error common to all of the qualitative and interactive density measurement techniques.

Recently, a system to automate this process has been presented. This system uses the method of fuzzy connectedness. After identifying a region that is within the section of interest as a reference, the rest of the regions are then analyzed to see how strongly they 'hang together' with the reference. A so-called connectivity scene is created that shows the closeness of each region to the reference region. This can then be thresholded to segment the radiodense regions.

6.1 Summary of Accomplishments

This research presents a promising approach for performing automatic segmentation of digitized mammograms. The proposed algorithm operates completely automatically and autonomously. After initial pre-processing the system takes the digitized mammogram and segments the breast tissue from the film background. This process, unlike the automatic systems proposed in the literature, requires no knowledge of the region to segment. The system creates a binary mask template that allows future operation on only the tissue region of the digitized mammogram.

After the breast tissue is segmented from the background the algorithm analyzes the tissue region to find the radiodense tissue. The proposed method uses a constrained version of the Neyman-Pearson classifier. This classifier operates on knowledge of the underlying distributions that make up the tissue region of the mammogram. It is shown in

the research that an image can be modeled fairly accurately using a Gaussian random variable. Using this random variable model an initial threshold can be automatically calculated to allow estimation of statistics of the underlying distributions.

The algorithm varies the threshold based on the relationship of the local variance and a scaling parameter, α . This parameter is chosen to offset the estimation error from the initial threshold. It allows an adjustment from the pure Bayesian classifier to the mean of the greater estimated distribution. Using this threshold the radiodense tissue is segmented and quantified.

The research database consisted of 152 mammograms from FCCC that were scanned by our research team. These mammograms consist of 38 patients and four films per patient. After initial development of our algorithm a set of ten images were provided for validation by Dr. Celia Byrne, an expert radiologist. They consisted of ten CC views of different patients.

The proposed algorithm presented herein has been validated to work on the ten images that were provided. Validation of this algorithm was performed in two steps. The first step involved a blind classification attempt. Using only estimated parameters about the images a ranking was performed that ordered the images by increasing density. Once the blind classification was reported, Dr. Byrne provided the actual percentage of radiodense tissue.

With the associated percentage the second step of the validation could be performed. The algorithm was trained using one image and the tested using the remaining nine images of the validation data. Promising results were obtained for a single scaling parameter. Because the validation data set was so small, effective estimation of the

underlying distributions could not be made. To compensate for these inaccuracies the initial threshold was augmented. Using augmentation and three training images 90% of the validation images could be ranked with a single image that was not properly classified by the algorithm.

6.2 Recommendations for Future Work

The algorithm presented in this thesis is a first step towards developing a robust, completely automated system for characterizing breast density in mammograms. The following areas of research can foster the development of techniques towards achieving this goal:

Development of experimental/algorithmic techniques for developing a formal definition of breast density. Current research is especially hampered by the lack of a common, agreed-upon definition for breast density.

Incorporating features other than gray-level for segmenting radiodense tissue. The shape and location of the tissue, age of the patient, etc have to be incorporated into the algorithm. Texture-based segmentation methods are a fertile area of research.

Develop objective validation techniques for the algorithm – rather than subjective measures that rely on the expertise of a radiologist. Validation of mammogram segmentation techniques using magnetic resonance imaging shows considerable promise.

REFERENCES

1. R. A. Anderson, "Deaths: leading causes for 1999," *National Vital Statistics Reports*, Vol. 49, No.11, Centers for Disease Control, 2001.
2. S. H. Landis, T. Murray, S. Bolden and P. A. Wingo, "Cancer statistics," *CA Cancer Journal*, Vol. 48, pp. 6-29, 1998.
3. American Cancer Society, *Cancer Facts & Figures*, 2002
4. I. N. Bankman, Eds., *Handbook of Medical Imaging, Processing and Analysis*, Academic Press, 2000.
5. C. H. Chen, G. G. Lee, "On digital mammogram segmentation and microcalcification detection using multiresolution wavelet analysis," *Graphical Models and Image Processing*, Vol. 59, No. 5, pp. 349-364, 1997.
6. R. N. Strickland, "Wavelet transforms for detecting microcalcifications in mammograms," *IEEE Transactions on Medical Imaging*, Vol. 15, No. 2, pp. 218-229, 1996.
7. S. Yu, L. Guan, S. Brown, "Automatic detection of clustered microcalcifications in digitized mammogram films," *Journal of Electronic Imaging*, Vol. 8, No. 1, pp. 76-82, 1999.
8. L. Tarassenko, P. Hayton, N. Cerneaz, M. Brady, "Novelty detection for the identification of masses in mammograms," *Proceedings of the 4th IEEE Int. Conf. on Artificial Neural Networks*, pp. 442-447, Cambridge, UK, 1995.
9. N. Karssemeijer, "Adaptive noise equalization and recognition of microcalcifications in mammograms," *Int. J. Pattern Recognition and Artificial Intelligence*, Vol. 7, No. 6, pp. 1357-1376, 1993.
10. R. Highnam, M. Brady, R. English, "Detecting film-screen artifacts in mammography using a model-based approach," *IEEE Transactions on Medical Imaging*, Vol. 18, No. 10, pp. 1016-1024, 1999.
11. P. Taylor, S. Hajnal, M-H. Dilhuydy, B. Barreau, "Measuring image texture to separate 'difficult' from 'easy' mammograms," *The British Journal of Radiology*, Vol. 64, pp. 456-463, 1994.
12. J. L. Kelsey and M. Gammon, "The epidemiology of breast cancer," *CA Cancer Journal*; Vol. 41, pp. 146-165, 1991.
13. C. Byrne, "Studying mammographic density: implications for understanding breast cancer," *Journal of the National Cancer Institute*, Vol. 89, pp. 531-533, 1997.
14. A. M. Oza and N. F. Boyd, "Mammographic parenchymal patterns: a marker for breast cancer risk," *Epidemiologic Reviews*, Vol. 15, pp. 196-208, 1993.
15. N. F. Boyd, J. W. Byng, R. A. Jong, E. K. Fishell, L. E. Little, A. B. Miller, G. A. Lockwood, D. L. Tritchler, M. J. Yaffe, "Quantitative classification of mammographic densities and breast cancer risk: results from the Canadian

- National Breast Screening Study," *Journal of the National Cancer Institute*, Vol. 87, No. 9, pp. 670-675, 1995.
16. N. F. Boyd, G. A. Lockwood, J. W. Byng, D. L. Tritchler and M. J. Yaffe, "Mammographic densities and breast cancer risk," *Cancer Epidemiology, Biomarkers and Prevention*, Vol. 7, pp. 1133-1144, 1998.
 17. J. N. Wolfe, "Breast Patterns as an index of risk of developing Breast Cancer," *American Journal of Roentgenology*, Vol. 126, pp. 1130-1139, 1976.
 18. J. N. Wolfe, "Risk of Breast Cancer development determined by Mammographic Parenchymal pattern," *Cancer*, Vol. 37, pp. 2486-2492, 1976.
 19. N. F. Boyd, H. M. Jensen, G. Cooke, H. Lee Han, "Relationship between mammographic and histological risk factors for breast cancer," *Journal of the National Cancer Institute*, Vol. 84, pp. 1170-1179, 1992
 20. M. J. Yaffe, N. F. Boyd, J. W. Byng, R. A. Jong, E. Fishell, G. A. Lockwood, L. E. Little, D. L. Tritchler, "Breast cancer risk and measured mammographic density," *European Journal of Cancer Prevention*, Vol. 7 (suppl 1), pp. S47-S55, 1998.
 21. B. B. Mandelbrot, *The Fractal Geometry of Nature*, W.H. Freeman, 1982.
 22. K. R. Castleman, *Digital Image Processing*, Prentice-Hall, 1996.
 23. M. J. Yaffe, J. W. Byng, N. F. Boyd, "Quantitative image analysis for estimation of breast cancer risk," *Handbook of Medical Imaging, Processing and Analysis*, Ch. 21, Academic Press, 2000.
 24. P. K. Saha, J. K. Udupa, E. F. Conant, D. P. Chakraborty and D. Sullivan, "Breast tissue density quantification via digitized mammograms," *IEEE Transactions on Medical Imaging*, Vol. 20, No. 8, 2001.
 25. J. Suckling, D. R Lewis and S. G. Blacker, "Paranchymal delineation by human and computer observers," 2nd *International Workshop on Digital Mammography*, A.G. Gale et al., Eds., York, UK 1994.
 26. R. Highnam, M. Brady, and B. Shepstone, "A representation for mammographic image processing," *Medical Image Analysis*, Vol. 1, pp. 1-18, 1996.
 27. J. W. Byng, N.F. Boyd, E. Fishell, R. A. Jong and M. J. Yaffe, "Quantitative analysis of mammographic densities," *Phys. Med. Biol.*, Vol. 39, pp. 1629-1638, 1994
 28. J. W. Byng, N. F. Boyd, E. Fishell, R. A. Jong and M. J. Yaffe, "Automated analysis of mammographic densities," *Phys. Med. Biol.*, Vol. 41, pp, 909-923, 1996.
 29. J. W. Byng, N. F. Boyd, L. Little, et al, "Symmetry of projection in the quantitative analysis of mammographic images," *European Journal of Cancer Prevention*, Vol. 5, pp. 319-327, 1996.
 30. Y. Viniotis, *Probability and Random Processes for Electrical Engineers*, McGraw-Hill, 1998.

31. J. S. Lim, *Two-Dimensional Signal and Image Processing*, Prentice Hall, 1989.
32. T.K. Moon and W. C. Stirling, *Mathematical Methods and Algorithms*, Prentice Hall, 2000.
33. G. Wentz, *Mammography for Radiologic Technologists*, McGraw-Hill, 1997.
34. Mammographic Image Analysis Society (MIAS),
<http://www.wiau.man.ac.uk/services/MIAS/MIASweb.html>
35. University of South Florida DDSM: Digital Database for Screening Mammography, <http://marathon.csee.usf.edu/Mammography/Database.html>
36. National Information Display Laboratory,
http://www.nidl.org/tech_clinicaleval.shtml
37. Lawrence Livermore National Laboratories (LLNL) and University of California at San Fransisco (UCSF) Database,
<http://figment.csee.usf.edu/Mammography/OtherResources.html#LLNL>
38. The CALMA Database (Computer Assisted Library in Mammography),
http://calma1.difi.unipi.it/calma_database.html
39. Macromedia, Inc., <http://www.coldfusion.com/>
40. G. Strang and T. Nguyen, *Wavelets and Filter Banks*, Wellesley-Cambridge Press, 1996.
41. J. Neyhart, M. Kirlakovsky, S. Mandayam and M. Tseng, "Automated segmentation and quantitative characterization of radiodense tissue in digitized mammograms," *Proceedings of the 28th Annual Review of Progress in Quantitative NDE*, American Institute of Physics, New York, July 2001.
42. J. Neyhart, M. Ciocco, R. Polikar, S. Mandayam and M. Tseng, "Dynamic segmentation of breast tissue in digitized mammograms using the discrete wavelet transform," *Proceedings of the 23rd Annual International Conference of the IEEE Engineering in Medicine and Biology Society*, Istanbul, Turkey, October 2001.

APPENDIX: MATLAB CODE

The following appendix contains all of the code used to operate the proposed algorithm on a single image. This code was written using MATLAB Version 6 Release 12 research edition with a full suite of toolboxes.

The following code will dynamically generate a binary mask. This mask is then saved so that the other code can call the image at any time without having to rerun this code.

```
function toolman = maskmake3(image_name)
%%%%%%%%%%%%%%%%%%%%%%%%%%%%%%%%%%%%%%%%%%%%%%%%%%%%%%%%%%%%%%%%%%%%%%%%
%
% This program will dynamically determine an edge/mask
% for a digitized mammographic image using a db5 wavelet
%
% Jeremy Neyhart, Mike Ciocco, Robi Polikar
% Rowan University 2001
%
% THIS VERSION FOR USE WITH BATCH IMAGE FILE OTHERWISE
% IDENTICAL TO MASKMAKE2.M
%
% v1.1 - added histogram equalization to image after
%       edge blanking process takes place
%
% V1.2 - added polyfit edge smoothing and edge line
%       generation. added forced zeros to top 5% of
%       image also
%%%%%%%%%%%%%%%%%%%%%%%%%%%%%%%%%%%%%%%%%%%%%%%%%%%%%%%%%%%%%%%%%%%%%%%%

% read in image
image_file = image_name(1:10);
image = imread(image_name);

% get size of original image
[m n o] = size(image);

% we want n to be 1600 so...
image = imresize(image,1600/n);

% convert from grb to gray
if o = 3
image = rgb2gray(double(image));
end

% convert to indexed
image = mat2gray(image);
```

```

% get the size of the image so we know how many rows to operate on
% we already know that n = 1600
[m n] = size(image);

% forces a histogram adjustment that increases contrast in image
im = imadjust(image,[0.01 0.11],[0 1]);

% for normalization purposes make the top and bottom 5% of rows and right 33% of columns = 0
% to eliminate the presense of name markers and curves in x-ray
% NOTE: None of the images used contained tissue in this region!!!
for k = floor(0.90*m) : m

    im(k,:) = 0;
end

for k = 1 : floor(0.10*m)

    im(k,:) = 0;
end

for d = floor(0.66*n) : n

    im(:,d) = 0;
end

% perform the wavelet analysis on each line of the image
% and construct an approximation image
for i=1 : m

    % get the line to operate on
    im_line = im(i,:);

    % perform the DWT
    [C L] = wavedec(im_line, 5, 'db5');

    % get the approximation
    line_a1 = C(1:L(1));

    approx_image(i,:) = line_a1;

end

% convert approximation image to a 0 to 1 scale
approx_image = approx_image/max(max(approx_image));

% value of threshold for approximation
threshold = 0.95;

% using the threshold look at each pair of values
% and determine the approximate point where the threshold is crossed
for k = 1 : m

```

```

% initialize the edge variable
edge = 1;

% load the next image line
line_approx = approx_image(k,:);

for j = 1 : length(line_approx)

    % if the pair contains the threshold
    if ((line_approx(j) > threshold) & (line_approx(j+1) <= threshold))

        % these lines interpolate where the threshold is crossed
        Q = line_approx(j)-line_approx(j+1);
        W = threshold - line_approx(j+1);
        E = W/Q;
        R = (j+1) - E;
        %R = j;
        % This tells where the edge is
        edge = floor(1600*(R/length(line_approx)));
    end
end

% knowing the edge point make a line going low at that point
mask_line(1:edge) = 1;
mask_line(edge:n) = 0;

% add it to the mask image
mask(k,:) = mask_line;

% creat graph of edge
mask_plot(k) = edge;

end

% create polyfit of the mask edge graph
X = [1:length(mask_plot)];
[P S] = polyfit(X,mask_plot,8);
Y = polyval(P,X);

% create the other mask
for q = 1:length(Y)
    edge_new = 1;

    if floor(Y(q)) > 1
        edge_new = floor(Y(q));
    end

    % creating the new mask image
    mask_line_new(1:edge_new) = 1;
    mask_line_new(edge_new:n) = 0;
    mask_new(q,:) = mask_line_new;
end
end

```


This code Calculates the Constrained Neyman-Pearson threshold then segments

the image and returns the percentage of radiodense tissue and the segmentation threshold.

```
function [prct_rd, t_np] = NM_analysis(im_in, thresh, a, blk_size)
%% %% %% %% %% %% %% %% %% %% %% %% %% %% %% %% %% %% %% %% %% %% %% %% %% %% %% %% %%
%%
% Jeremy Neyahrt - Rowan University
% Spring 2002
%
% This program will calculate the average
% mean and average variance of the radiodense
% and radiolucent regions of an image then
% use the constrained Neyman-pearson method to determine the
% percentage of radiodense tissue in the image
%
%
%% %% %% %% %% %% %% %% %% %% %% %% %% %% %% %% %% %% %% %% %% %% %% %% %% %% %% %% %%

if nargin == 0
    im_in = input('Enter Image name: ');
    thresh = input('Enter threshold: ');
    blk_size = input('Enter block size: ');
    a = input('Enter alpha: ');
elseif nargin == 1
    thresh = input('Enter Threshold: ');
    blk_size = [8 8];
    a = input('Enter alpha: ');
elseif nargin == 2
    blk_size = [8 8];
    a = input('Enter alpha: ');
elseif nargin == 3
    blk_size = [8 8];
end

im_in

im = imread(im_in);
im = mat2gray(double(im),[0 255]);

im_mask = imread([ im_in(1:8) '_mask2.bmp']);
im_mask = mat2gray(double(im_mask));

% see if it's a model image or original
% orig has 12 chars in name & you need mask
if length(im_in) > 12
    im_mask = double(blk_rd_fun(im_mask));
end

im = im.*im_mask;

% generate an image with only the radiodense tissue all else = 0
rd = double(im2bw(im,thresh));
rd_area = length(find(rd==1));
```

```

im_rd = im.*rd;

% generate an image with only the nonradiodense tissue all else = 0;
nrd = double(abs(rd - 1).*im_mask);
nrd_area = length(find(nrd==1));
im_nrd = im.*nrd;

% generate mean and variance matrixs
im_rd_mean = blkproc(im_rd, blk_size,'mean_fun');
im_nrd_mean = blkproc(im_nrd, blk_size,'mean_fun');
im_var = blkproc(im, blk_size,'var_fun');

% calculate the average mean and variance
m1 = sum(sum(im_nrd_mean))/nrd_area;
m2 = sum(sum(im_rd_mean))/rd_area;
s = sum(sum(im_var))/(prod(size(im)) - length(find(im_mask == 0)));

t_np=(m2+m1)/2 + ((a-s)/a)*((m2-m1)/2);
%im_np=blkproc(im,[1 1],'neyhart_mandayam',m1,m2,s,a);
im_np=double(im2bw(im,t_np));
im_np = im_np.*im_mask;

prct_rd = 100*(length(find(im_np ==1))/(prod(size(im_np)) - length(find(im_mask == 0))));

```